A Power Class Interoperable Multi-Coil Inductive Power Transfer System for 10/50 kW EV Charging

Patrick A. J. Lawton, *Student Member, IEEE*, Feiyang J. Lin, *Member, IEEE*, and Grant A. Covic, *Senior Member, IEEE*

Abstract This paper presents an Inductive Power Transfer (IPT) system for Electric Vehicle (EV) charging with Power Class Interoperability (PCI) between the SAE WPT3 (10 kW) and WPT5 (50 kW) power classes using a multi-coil Bi-Polar Pad (BPP) Vehicle Assembly (VA) magnetic topology. The objective is to provide wireless PCI for electric taxis and fleet vehicles which may require WPT5 charging while on shift and WPT3 off shift charging. The design process of the WPT3/5 BPP VA magnetics is presented. Alternative methods of ferrite core layout and coil overlap to reduce form factor and cross-coupling are investigated. A dual active bridge topology using LCC-LCC tuning demonstrates effective dual-sided control, combining conduction angle, active bridge phase shift, and Selective Coil Energization (SCE) to provide system functionality essential to PCI. Active bridge phase shift is utilized to adjust the relative secondary to primary phase past 90° to enable Zero-Volt Switching (ZVS) in the active bridges when operating at either power class. Experiments demonstrate the proposed WPT3/5 BPP VA charging from an above ground WPT3 UGA, and flush ground mounted WPT5 GA, and show an efficiency increase of 3.6% and 0.7% respectively when the proposed control method is used. The performance of the proposed system is shown to be comparable to other IPT systems at either power class.

***Index Terms*— Inductive power transfer, high power, electric vehicle charging, multi-coil, interoperability, wireless power transfer**

I. Introduction[1]

WIRELESS charging of EVs with IPT has been standardized by SAE J2954 at low-power levels and is expected to become an industry alternative to plug-in charging [1]. The standard provides recommended designs for wireless charging systems with an input rating of up to 11 kVA (WPT3). A future version will provide recommendations for high-power (fast-charging) systems with an input rating of up to 60 kVA (WPT5), to provide a wireless alternative for plug-in fast-charging [1]. Commercial Electric Fleet Vehicles (EFV) such as taxis and delivery vehicles which require charging in public areas will gain increased range and functionality from wireless fast-charging [2]-[5]. Ideally, they can charge at a lower rate at a domestic residence or depot, and be able to benefit from fast-charging where available.

Over the last two decades there has been extensive research into IPT magnetic topologies for EV charging [6]-[14]. These range from the single-coil non-polarized Circular Pad (CP) and the polarized Double-D Pad (DDP) [6]-[8], to more complex but highly functional multi-coil and multi-phase designs such as the Bi-Polar Pad (BPP) [9], DDQP topology [10], Tri-Polar Pad (TPP) [12], and three-phase designs [11], [13]-[14].

Existing literature investigates how effectively one type of magnetic topology interacts with another, referred to as magnetic interoperability [15]-[20]. An example is two IPT systems where the Ground Assembly (GA) and Vehicle Assembly (VA) magnetics are matched: System-1 is designed as a DDP-DDP (GA-VA), and System-2 is a CP-CP. If they are interoperable, the System-1 VA can charge from the System-2 GA and vice versa. This means the resulting magnetic and electrical characteristics of the transposed system operates within the limits of the individual systems.

Aside from magnetic topology mismatches, the inability of a single system to adequately meet the needs of wireless PCI is the most significant limitation of current wireless charging technology. EFVs which are privately owned (e.g. taxis and couriers), are common examples where power class interoperability is essential. A WPT5 VA is ideal for opportunity charging at taxi-ranks or goods depots with a commercial WPT5 GA. However, designing a WPT5 VA to charge over a WPT3 GA is challenging. This scenario is explored and its solution is a novel contribution of this article.

The first challenge of PCI is the difference between magnetics for low and high-power charging. As the power class increases, so does the relative size of the magnetics [2]-[6]. Having a size mismatch causes a large range of magnetic coupling factors between the two pads ($k_{1,2}$), significant variations in self-inductance, and potentially increased magnetic flux leakage adjacent to the EV during charging [6].

The next challenge relates to the installation method of the GA which is shown in Fig. 1. Commercial and public fast-charging spaces usually prefer to install the pad flush with the ground surface. This prevents excessive wear on the pad and avoids additional driving obstacles. In contrast, a low-power GA at a residence will likely be surface mounted in a garage or driveway to reduce installation cost. While the ground clearance of the VA pad remains unchanged, the magnetic airgap can potentially halve, depending on the GA

Submitted using MS Word Template for review on 21 September 2024.
P. A. J. Lawton, F. J. Lin, and G. A. Covic are with the University of Auckland, Auckland, New Zealand. (e-mail: patrick.lawton@auckland.ac.nz, jackman.lin@auckland.ac.nz, and ga.covic@auckland.ac.nz).

This article has been accepted for publication in IEEE Open Journal of Power Electronics. This is the author's version which has not been fully edited and content may change prior to final publication. Citation information: DOI 10.1109/OJPEL.2024.3514519

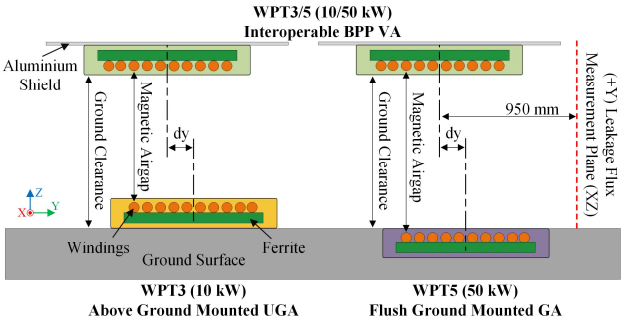

Fig. 1. Diagram (not to scale) of proposed WPT3/5 interoperable BPP VA charging over a WPT3 above ground mounted UGA and a WPT5 flush ground mounted GA.

pad thickness. This further strains the system operation given the large variations in coupling that neither the GA or VA were initially designed for.

The final challenge is in regard to the power electronics, power regulation/control mechanism, and volt-ampere rating mismatch of the two systems. WPT5 systems proposed in literature demonstrate volt-ampere ratings in excess of 2 to 4 times that of WPT3 systems [3], [8], [13]-[14]. Without relying on highly functional (and therefore expensive) dc-dc converters in the GA and/or VA battery management system, there must be other means of power regulation within the IPT system.

As more high-power IPT literature and candidate systems are produced, there has been growing interest in methods to address wireless PCI challenges [17], [20]-[21]. Table I lists and compares several examples of IPT literature that investigate this topic, or at least demonstrate a higher-power system operating at low-power.

Kim et al. proposed a method of Selective Coil Energization (SCE), for a 20 kW multi-coil TPP to facilitate operation with a high-power TPP VA and/or a low-power single-coil topology similar to those in SAE J2954 [12]. Kurpat and Eckstein proposed a three-phase 30 kW system with SAE J2954 WPT3 GA interoperability [17]. They investigated the magnetic interoperability of star/delta-type multi-coil topologies with single-phase CP and DDP GAs and the increased power density of a three-phase matched system through Finite Element Analysis (FEA).

Both of these works investigate the potential for high-power multi-coil magnetics to interoperate with low-power single-coil SAE J2954 magnetics. However, they do not experimentally prove their respective systems at both low-power and high-power operation or consider the power electronics topology and control methods required for PCI.

Pries et al. demonstrate a novel three-phase 50 kW system operating at reduced power level (10 kW), when misaligned, but with reduced system efficiency [13]. Ibrahim et al. also demonstrate a 50 kW three-phase system operating at a reduced power level (5 kW), which is achieved by only driving one of the three-coils on the GA with a significantly reduced dc bus voltage.

While these two examples demonstrate low-power operation of a high-power system is possible, neither are interoperable with SAE J2954 charging systems. They also operate with reduced system efficiency, and/or expect a wide range of control over the dc voltage input to the GA system.

Su et al. investigated a multi-coil to single-coil system [20], which uses a three-phase magnetics topology showcased in [13]. They proposed a single-phase mode of operation for a 50 kW three-phase active bridge when their three-phase magnetics are charging to, or from, a WPT3 CP/DDP. They demonstrated conceptually how power class interoperability can be facilitated from an electronics perspective. While not demonstrated experimentally, the authors provided simulated electrical operating characteristics which demonstrate a moderate power regulation requirement.

Torres-Alfonso et al. performed an interoperability study that investigated the challenges associated with variations in reflected impedance and power regulation [21]. They provided a conceptual design of an interoperable GA using simulations, but did not experimentally demonstrate their proposed GA as interoperable with low-power SAE systems.

The above literature shows initial analytical and simulated electrical/magnetic investigations that broaches the topic of power class interoperability. Despite this early work, research gaps remain regarding the practical implementation of a low/high-power SAE compliant system. The work in this paper presents the first literature to the authors knowledge, which considers the system challenges in all of the magnetic, electronic, and power regulation control environments, and demonstrates solutions that result in the practical implementation of a power class interoperable IPT system.

Of interest is how the volt-ampere rating mismatch in a wireless power class interoperability scenario is managed. From the previously discussed example (WPT3 GA to WPT5 VA), if the high-power VA cannot regulate its volt-ampere effort when positioned over a low-power GA, an alternative would be to rely on a very low magnetic coupling. This could be attempted during the high-power VA design, however the low magnetic airgap caused by the low-power GA mounting method may make this unrealistic. Therefore, it is more practical to assume the high-power VA will be capable of regulating its magnetic volt-ampere effort within range of the low-power GA rating.

TABLE I
IPT SYSTEMS DEMONSTRATING POWER CLASS INTEROPERABILITY*

Research Group	Power Levels	Magnetic Topology	SAE J2954 Compatible	Experimental Validation at Both Power Levels	Year
UoA [12]	2 kW and 20 kW	TPP	Yes	No	2019
Ika RWTH [17]	11 kW and 30 kW	Three-Phase	Yes	No	2019/2022
ORNL [13]	10 kW and 50 kW	Three-Phase	No	Yes	2020
ZJU [14]	5 kW and 50 kW	Three-Phase	No	Yes	2021
ORNL [20]	11 kW and 50 kW	Three-Phase	No	No	2023
CIRCE [21]	≤ 50 kW	CP	No	No	2023
UoA Proposed System	10 kW and 50 kW	BPP	Yes	Yes	2023

*or at least demonstrating a high-power system operating at low-power.

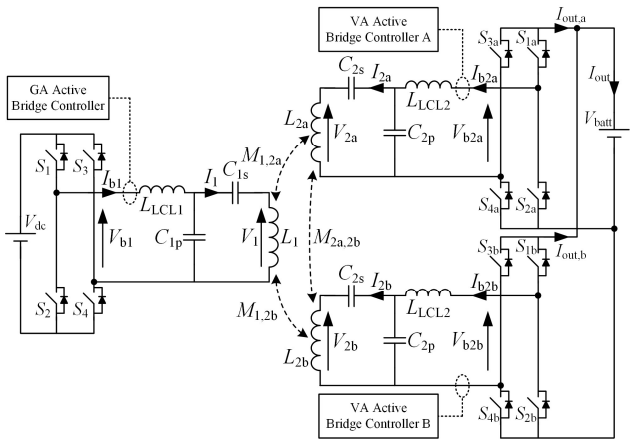

Fig. 2. Schematic diagram of the WPT3/5 dual-side control active bridge LCC-LCC IPT system used in this work. All active bridge legs are CAS120M12BM2 modules.

In the context of power class interoperability, a balanced multi-coil VA that is able to short or open circuit one or more of its windings (SCE) is immediately at an advantage compared to an equivalent single-coil VA. This allows the volt-ampere rating of the VA system to be significantly dropped prior to engaging power regulation [12].

Methods of power regulation within IPT systems, which inherently regulate the volt-ampere effort of the GA and/or VA magnetics, are showcased in the literature, and a variety of solutions are presented in [22]-[31]. Conduction angle control (α-control) within the GA does not require additional hardware other than an active dc-ac bridge, and is arguably the most common approach. Dual-side control makes additional use of active switching on the VA side to also regulate power.

Dual-side control can take the form of a robust dc side regulator [22]-[23], to a sophisticated semi/full-bridge active rectifier with VA side α-control and/or phase-shift control (φ-control) of the VA active bridge relative to the GA [24]-[31]. The cost of dual-side control is higher than single-sided power regulation techniques. However, the increased component cost can be reduced as dual-side control is able to exploit Zero-Voltage Switching (ZVS) in the GA and/or VA active bridges [24]-[29], [31].

The main contribution of this work is a power class interoperable multi-coil BPP VA suitable for WPT3/5 (10/50 kW) charging at high efficiency, which is compatible with SAE J2954 low-power IPT charging systems. This is achieved using selective coil energization of the multi-coil VA, and using a dual-sided control strategy to improve the efficiency of the system while meeting leakage flux constraints.

The operation of the proposed BPP VA (Fig. 1), is evaluated when charging at a WPT3 level from an above ground mounted single-coil SAE J2954 Universal Ground Assembly (UGA) [1]. WPT5 charging is also evaluated with a single-coil CP GA which is designed to be flush with the ground surface [32]. This is a challenging power class interoperability scenario where there is a significant difference in magnetic coupling and volt-ampere ratings of the two individual systems.

The decisions regarding initial system specifications, such as magnetic misalignment, the primary side dc bus, the secondary side battery voltage range, and leakage flux are discussed. The design method of the BPP WPT3/5 VA magnetics, which includes magnetic core design, winding overlap, and inter-coil cross-coupling reduction methods, are also detailed.

TABLE II
PROPOSED WPT3/5 SYSTEM DESIGN CONSTRAINTS

General System Parameters			
Parameter	Value	Parameter	Value
$V_{dc\ (10kW)}$	380-500 V	$B_{leakage}$	15 μT
$V_{dc\ (50kW)}$	600-800 V	dx	±75 mm
V_{batt}	800 V	dy	±100 mm
$B_{ferrite,max}$	90 mT	dz[1]	160-210 mm
WPT5 Operation Over 50 kW CP GA			
V_1	2 kV	V_{2m}	2 kV
I_1	200 A	I_{2m}	130 A
VA_1	400 kVA	VA_{2m}	260 kVA
L_1	18.7 uH	L_{2m}	28.8 uH
$k_{1,2(eff)min}$	0.125	$\Delta k_{1,2(eff)}$	≤ 0.12
$k_{1,2m(min)}$	0.05	Q_{2m}	15
WPT3 Operation Over 10 kW UGA			
V_1	1.6 kV	L_1	39.4 uH
I_1	75 A	VA_1	118 kVA

[1] Ground clearance airgap as per Fig. 1.

The power class interoperability limitations of a WPT5 single-coil VA are discussed, and the advantages of a multi-coil VA with selective coil operation for power class interoperability are demonstrated.

Even with selective coil energization, a moderate power regulation effort from the GA and VA active bridges is required to operate over the wide power class range. A dual-sided control strategy that regulates power through both α and φ-control to regulate the volt-amperes in the magnetics is used in this work. Control actions that adjust φ-control past -90° (φ-overdrive) are demonstrated to improve system efficiency and increase the ZVS range of the active bridges by modifying the reflected impedance of the LCC-LCC system [24]-[25]. The dual-sided control strategy is shown to be beneficial across the proposed power classes via experiments.

A prototype WPT3/5 BPP VA is built, tested, and experimental results are presented that show the prototype can transfer rated power at system ratings while complying with specifications. The performance of the proposed system is compared with respective low-power and high-power IPT systems described in the literature. Results are discussed, and further recommendations are made regarding dual-action control for power class interoperable IPT systems.

II. WPT3/5 (10/50 KW) INTEROPERABLE IPT SYSTEM SPECIFICATIONS

This section discusses the electrical and magnetic parameters that were used to constrain the design of the VA BPP magnetics. These constraints were chosen based on existing literature for WPT5 IPT systems [3], [8], [13]-[14], however the main guiding factors are the design constraints that developed the 50 kW single-coil system in the authors previous works [32]. SAE J2954 recommends specifications for WPT3 rated IPT EV charging systems [1]. These works are combined

to propose the WPT3/5 (10/50 kW) interoperable system design constraints, which are shown in Table II

A diagram of the proposed interoperable system is shown in Fig. 2, where the VA has two receiver coils (L_{2a} and L_{2b}), and synchronized active bridge regulators to deliver power to the battery. When the multi-coil VA is charging over a WPT5 GA, both L_{2a} and L_{2b} deliver power. When charging over a WPT3 GA, only one coil in the VA is needed to deliver power and the other is short-circuited by the respective active bridge. The SCE operation is discussed in Section II-E.

A. General System Operation

The range of the GA dc bus voltage (V_{dc}) for WPT3 charging is 380-500 V based on SAE specifications for the UGA testing system. This is extrapolated to define a V_{dc} range of 600-800 V for WPT5 operation, based on the referenced WPT5 system V_{dc} maximum of 800 V [32].

The EV battery voltage (V_{batt}) is 800 V as per [32]. It is assumed the battery management system maintains a constant 800 V dc load on the output of the proposed IPT system and does not fluctuate with the EV state of charge.

Misalignment of the VA in the XY plane (*dx*,*dy*) and ground clearance airgap (*dz*) are taken from SAE specifications (Fig. 1) [1]. Due to the different mounting methods, there is a significant difference in magnetic airgap, which is shown by Fig. 1. When charging from the WPT3 UGA, the magnetic airgap is reduced by approximately 62 mm for a given *dz* ground clearance. This results in a sharp increase in coupling which the proposed multi-coil BPP VA compensates for by reducing its volt-ampere rating through SCE.

Maximum leakage flux adjacent to the EV during charging ($B_{leakage}$) is set at 15 μT to comply with cardiac implantable electronic device requirements [1]. The measurement location is 950 mm from the VA center (as discussed in [32] given the typical vehicle widths), under maximum misalignment and power transfer conditions. This $B_{leakage}$ maximum usually occurs in the XZ plane along the Y-axis as shown by Fig. 1.

B. Coupling Factor and Power Transfer Equations

In order to simplify the power transfer analysis of a multi-coil IPT system, a metric called the effective coupling factor ($k_{1,2(eff)}$) is used during the design stage [12]. For the purposes of this work, $k_{1,2(eff)}$ is used to evaluate the proposed WPT3/5 multi-coil magnetics as an equivalent single-coil system.

The proposed WPT3/5 BPP VA magnetics have two separate coil windings L_{2a} and L_{2b}, which are individually coupled with the GA magnetics (L_1). (1) describes the subsequent mutual-inductance ($M_{1,2m}$ where $m \in \{a,b\}$) between L_1 and either L_{2a} or L_{2b} as a function of their respective magnetic coupling ($k_{1,2m}$) and self-inductance (L_{2m}). (2) describes the open-circuit voltage induced in the respective VA coils, and (3) describes the volt-ampere effort (VA_1, or VA_{2m}) as a function of the current (I_1 or I_{2m}) in the respective winding.

Using (1) through (3), (4) can be derived which describes the power output of the respective active bridge ($P_{out,2m}$) as a function of the coupling, volt-ampere effort of the GA and respective VA winding, and the phase shift between the GA and VA winding current (θ).

$$M_{1,2m} = k_{1,2m}\sqrt{L_1 L_{2m}} \tag{1}$$

$$V_{oc1,2m} = j\omega I_1 M_{1,2m} \tag{2}$$

$$VA_1 = |I_1|^2|j\omega L_1|,\ VA_{2m} = |I_{2m}|^2|j\omega L_{2m}| \tag{3}$$

$$P_{out,2m} = k_{1,2m}\sqrt{VA_1 VA_{2m}}\sin(\theta) \tag{4}$$

The uncompensated volt-amperes coupled to L_{2a} or L_{2b} (Su_{2m}) is shown by (5) as a function of the power output by the respective active bridge $P_{out,2m}$, and the loaded quality factor of its resonant tuning network (Q_{2m}). By substituting (1) and (3), (5) can be expressed as a function of the volt-ampere effort of L_1 and its magnetic coupling with L_{2a} or L_{2b}.

$$Su_{2m} = \frac{P_{out,2m}}{Q_{2m}} = I_1^2 \omega \frac{M_{1,2m}^2}{L_{2m}} = VA_1 k_{1,2m}^2 \tag{5}$$

The total output power of the IPT system is the sum of the two secondary side active bridges (Fig. 2), as is the total uncompensated power available from L_{2a} and L_{2b} which is shown by (6). Using (5), (6) can be expanded into (7), which is simplified to provide (8), which describes $k_{1,2(eff)}$.

$$Su_{eff} = Su_{2a} + Su_{2b} \tag{6}$$

$$VA_1 k_{1,2(eff)}^2 = VA_1 k_{1,2a}^2 + VA_1 k_{1,2b}^2 \tag{7}$$

$$k_{1,2(eff)} = \sqrt{k_{1,2a}^2 + k_{1,2b}^2} \tag{8}$$

Under maximum misalignment and ground clearance, the minimum effective coupling ($k_{1,2(eff)min}$) should be close to 0.125, and the difference between minimum and maximum effective coupling ($\Delta k_{1,2(eff)}$) should be 0.12. These are the same coupling factor specifications the referenced single-coil WPT5 system was designed to, the performance of which is compared to the WPT5 operation of the proposed BPP VA at the end of Section VII [32].

C. Electrical and Magnetic Operating Limits

The BPP coil terminal voltage limit (V_{2m}) is set at 2 kV which is identical to the single-coil CP voltage limit (V_1) as per [32]. The available Litz wire size of 4800x0.1 mm provides an effective conductor area of 37.7 mm^2, which should have a current density of less than 4 A/mm^2 in an enclosed prototype IPT pad with no active cooling. This limits the current in the single-filar BPP coils (I_{2m}) to 150 A. A conservative value of 130 A is chosen to allow some freedom in the design stage.

The chosen V_{2m} and I_{2m} limits produce identical BPP L_{2a} and L_{2b} self-inductances of 28.8 μH and a maximum volt-ampere effort of 260 kVA. The WPT5 GA characteristics remain unchanged from [32] and are also listed in Table II.

The minimum couplings between L_1 and either L_{2a} or L_{2b} ($k_{1,2m(min)}$) must be high enough to avoid operating the VA tuning network at an excessive loaded Q_2, which causes the VA to become sensitive to changes in the resonant tuning network values. Q_{2m} and $k_{1,2m(min)}$ can be related by substituting (5) into

TABLE III
SIMULATION OF WPT5 CP OVER WPT3 UGA UNDER MAXIMUM COUPLING AND VA SIDE POWER REGULATION*

(dx,dy,dz) (mm)	$k_{1,2}$	$(\alpha_1, \alpha_2, \varphi)$ (°)	$P_{(out)}$ (kW)	$\eta_{dc\text{-}dc}$ (%)	I_1 (A)	I_2 (A)	VA_1 (kVA)	VA_2 (kVA)	I_{b1} (A)	I_{b2} (A)	S_u (kVA)	Q_2	GA $I_{S(on)max}$ (A)	VA $I_{S(on)max}$ (A)
(0,0,160)	0.381	(180,14,-90)	10.5	84.5	73.6	31.6	113.9	9.2	46.9	112.4	16.8	0.6	29.3	135.1

*V_{dc} = 380 V and V_{batt} = 800 V

(4) and solving for $k_{1,2m(\min)}$ to produce (9).

$$k_{1,2m(\min)} = \sqrt{\frac{VA_{2m}}{VA_1}}\frac{1}{Q_{2m}} \tag{9}$$

As the GA and VA active bridges are synchronized, ideally with a 90° phase difference (see Section V), the sin(θ) term in (4) can be approximated as 1. If Q_{2m} is limited to a maximum of 15, a $k_{1,2m(\min)}$ of 0.05 can be calculated using (9).

D. LCC-LCC Tuning and DAB Topology

An LCC-LCC tuning topology was chosen for the proposed power class interoperable IPT system as it provides a nearly constant current (and therefore volt-amperes), within the magnetics irrespective of coupling and/or loading conditions, and its band pass filtering of the ac voltage output from the respective active bridge. These features are desirable as this system will inherently have a wide range of coupling/loading conditions, and require low conduction angles in the active bridges (high harmonics in the ac voltage outputs), to provide a moderate level of power regulation.

The decision to employ a DAB topology was to allow SCE of the proposed BPP for WPT3 operation, and to provide a high level of control functionality (conduction angle and active bridge phase shift), the necessity of which is demonstrated in Section VI.

E. Selective Coil Energization (SCE) WPT3 Operation

As noted in Fig. 2, either of coil L_{2a} and L_{2b} can be stopped from operating under resonance, and delivering power, by closing switches $S_{2a/b}$ and $S_{4a/b}$. When either set of switches are closed there is an effective short circuit current that flows which is greater than the actual coil short circuit current, because of C_{2s}. The effective short circuit currents ($I_{sc(eff)m}$) are thus given by (10). Under these conditions, the bridge currents I_{b2m} are equal to $I_{sc(eff)m}$.

By substituting (1) and (2) into (10), the coupling between L_1 and each respective VA winding can then be estimated by (11). The VA controller has information regarding $I_{sc(eff)m}$ and $X_{L2m(eff)}$, while the GA communicates ω, I_1, and L_1 via wireless communication. The VA controller may then decide to energize L_{2a} or L_{2b} based on which has the more appropriate coupling to the WPT3 GA magnetics.

$$\left|I_{sc(eff)m}\right| = \frac{|V_{oc1,2m}|}{|X_{L2m}|-|X_{C2s}|} = \frac{|V_{oc1,2m}|}{|X_{L2m(eff)}|} \tag{10}$$

$$k_{1,2m} = \frac{|I_{sc(eff)m}|\,|X_{L2m(eff)}|}{\omega I_1\sqrt{L_1 L_{2m}}} \tag{11}$$

If the detected coupling is outside the operating range of the system this indicates the EFV is severely misaligned from the GA magnetics. The charging system would prompt the driver to reposition the vehicle before charging can occur. The revised SAE J2954 standard will contain details on positioning systems which will assist the driver, or automated parking system, with EV alignment to reduce the likelihood of severe misalignment occurring. [1].

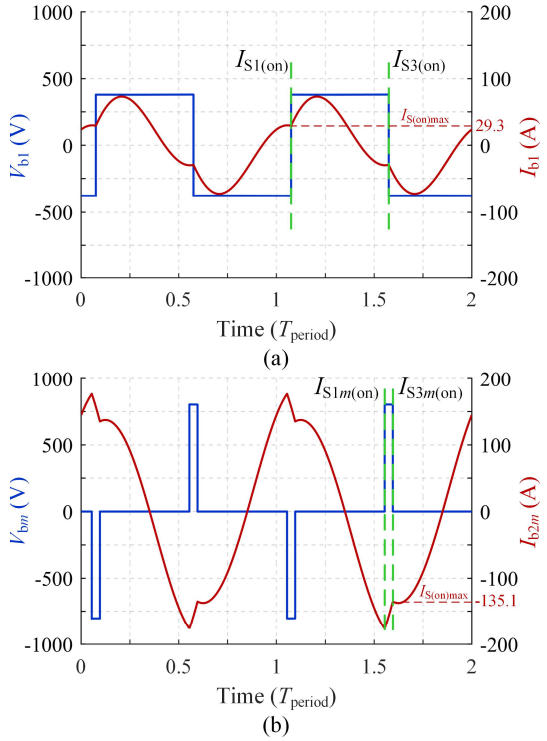

Fig. 3. Simulated ac bridge voltage (blue) and current (red) waveforms as per Table III, with current flow directions as per Fig. 2. Green dashes mark S_1 and S_3 switching transitions where $I_{S(on)}$ is recorded. (a) GA active bridge (b) VA active bridges.

F. Multi-Coil VA Necessity for WPT3 Interoperability

Table III details a PLECS simulation of the single-coil WPT5 CP VA from [32] charging from the WPT3 UGA with (dx,dy,dz) = (0,0,160) mm. The simulated waveforms of the ac bridge voltage and currents for the GA and VA active bridges are shown in Fig. 3(a) & (b) respectively.

In this simulation, the WPT3 active bridge operates with a 180° conduction angle (α_1), and regulates power by operating with its minimum V_{dc} of 380 V. The 180° conduction angle favors ZVS operating conditions in the WPT3 active bridge. A power output of approximately 10 kW is achieved by operating the synchronized WPT5 rated VA active bridge with a very low conduction angle (α_2 = 14°).

The high coupling results in the system operating with an uncompensated volt-ampere rating (Su), which is greater in magnitude than the desired 10 kW power output. Under these conditions, the loaded quality factor (Q_2) of the VA will be less than 1. This operates the system is a low resonance state which induces high harmonics in the ac-dc and dc-ac conversion

This article has been accepted for publication in IEEE Open Journal of Power Electronics. This is the author's version which has not been fully edited and content may change prior to final publication. Citation information: DOI 10.1109/OJPEL.2024.3514519

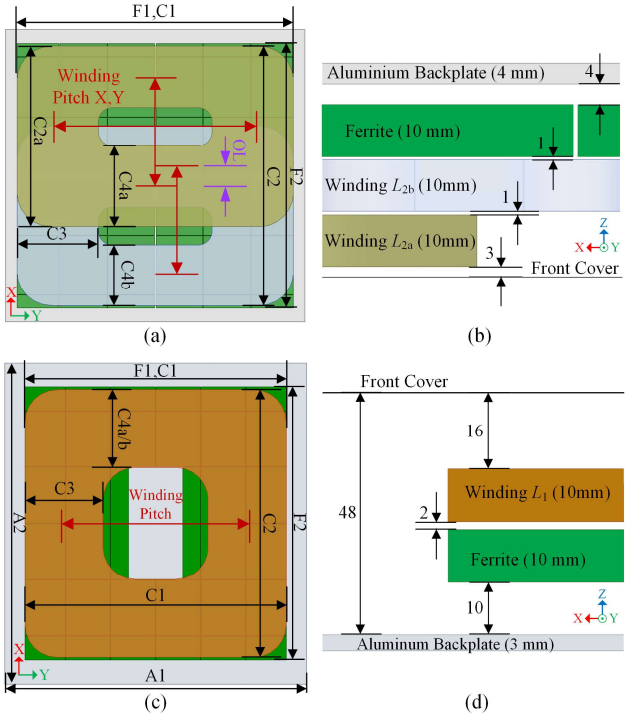

Fig. 4. WPT3/5 BPP VA magnetics (a) bottom view and (b) side view. WPT5 CP GA magnetics (c) bottom view and (d) side view. All dimensions are in mm.

process.

A low resonance state also produces unfavorable hard-switching conditions in the active bridges, shown by $I_{S(on)max}$ in Table III. The high forward current flow at the switching transitions (non-ZVS), is shown by the green dashed lines in Fig. 3. Note the negative I_{b2m} value in Fig. 3(b) is relative to the I_{b2m} direction indicated in Fig. 2. Therefore, a negative I_{b2m} value at the $S_{3m(on)}$ transition indicates downward (positive) current flow through switch S_3 within the VA active bridges.

Further lowering I_1 using conduction angle control in the GA in order to boost Q_2 is not practical, as this further increases the magnitude of hard-switching in the GA active bridge. Lowing V_{dc} further is also limited by the WPT3 GA hardware.

The low dc-dc system efficiency ($\eta_{dc\text{-}dc}$) of 84.5 % is attributed to the hard-switching in the GA and VA, and high magnitude bridge current in the VA (I_{b2}), which produces conduction losses which are disproportionate to the amount of power being transferred.

The limitations of single-sided power regulation is explored further in Section VI where the dual-sided control method for the proposed WPT3/5 system is presented.

III. WPT3/5 BPP Magnetics Design Process

The multi-coil BPP magnetics topology is applied in this work to facilitate power class interoperability, rather than the traditional application of magnetic interoperability with both polarized and non-polarized single-coil magnetics.

The principal challenge with designing power class interoperable VA magnetics is the large solution space for the individual power classes and the relatively small overlap of solutions that meets both sets of specifications.

A pragmatic approach is to focus on solutions for the higher power class, where the specifications are more challenging to meet, and then investigate their performance under the lower power class conditions. A benefit of this approach is it immediately gives an indication of the magnetic dimensions required to achieve the minimum $k_{1,2(eff)}$ required to transfer rated power under maximum misalignment conditions.

TABLE IV
Magnetics Dimensions in mm With Respect to Fig. 4(A)&(C)

Parameter	10/50 kW VA	50 kW GA	10 kW UGA
A1	633	675	750
A2	620	720	600
F1	585	585	650
F2	560	612	510
C1	585	585	650
C2	550	600	500
C2a	382	-	-
C3	172	175	175
C4a	172	175	175
C4b	129	175	175
Winding Pitch X	232	425	325
Winding Pitch Y	413	410	475
Overlap (OL)	42	-	-

The design input dimensions are shown in Fig. 4 (see Fig. 7 for a 3D view), while Table IV shows the design dimensions of the proposed WPT3/5 BPP VA, and the equivalent dimensions of the WPT5 GA and WPT3 UGA. Fig. 5 shows a flowchart that steps through the FEA design process, as discussed in the following sub-sections.

A. BPP Magnetics Design Process

This first consideration is the maximum outer dimensions of the pad defined by F1, F2, C1, and C2 as per Fig. 4(a). The outer dimensions were selected to match the WPT5 CP VA as per [32]. This maintains similar copper winding and ferrite core volume, which helps compare the WPT5 VA from [32] with this newly proposed VA.

The next consideration is the BPP VA coil cross-coupling which should ideally be decoupled but in practice, minimized i.e. $k_{2a,2b} < 0.01$ (referred to as k_{null}). If this condition is not met, some power is circulated between L_{2a} and L_{2b}, which decreases magnetic efficiency [9]. k_{null} occurs when the net mutual flux shared between L_{2a} and L_{2b} is almost zero [9]. The amount of Overlap (OL), required to achieve k_{null} depends on the winding pitch and ferrite core arrangement underneath the two coils.

As the ferrite core and outer dimensions of the coils are already fixed, C2a, C4a, and C4b are the design variables that directly affect $k_{2a,2b}$. As per Fig. 4(a) and Table IV, the design variables Winding Pitch X/Y and Overlap (OL), are defined by (12) through (14).

$$\text{Winding Pitch X} = \text{C2a} - (\text{C4a} + \text{C4b})/2 \quad (12)$$

$$\text{Winding Pitch Y} = \text{C1} - \text{C3} \quad (13)$$

$$\text{OL} = \left((\text{C4b}/2 + \text{Winding Pitch X}) - \text{C2}/2\right) \times 2 \quad (14)$$

With equal C4a & C4b dimensions, k_{null} occurs when the X-axis winding pitch of L_{2a} and L_{2b} overlap (OL) by approximately 20 % of Winding Pitch X (Table IV). However, in this design process, C4a/b dimensions are varied

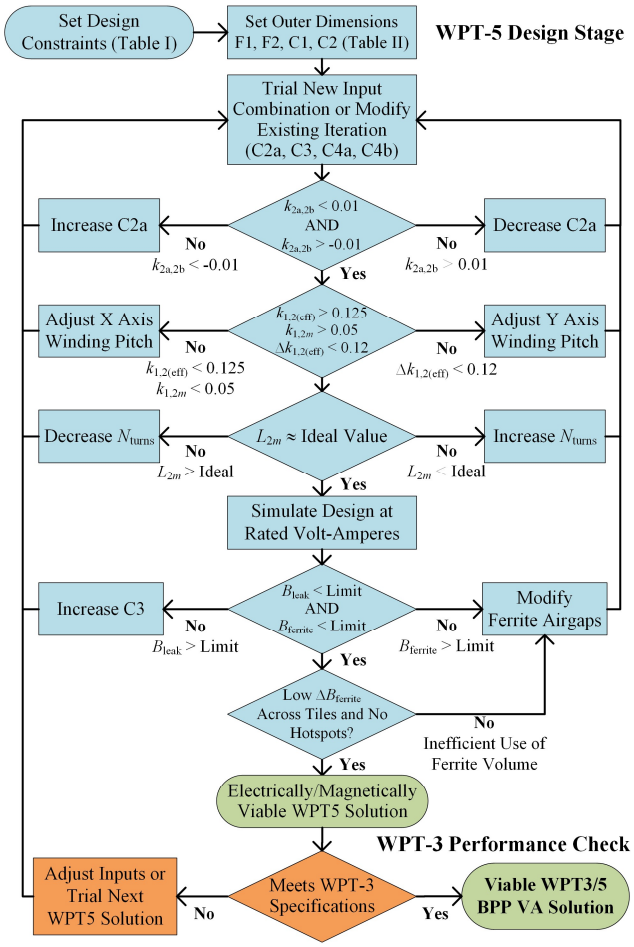

Fig. 5. WPT3/5 BPP VA magnetics design process flowchart.

independently to improve $k_{1,2(eff)}$. The ferrite core is made of ferrite tiles and thus is not symmetrical underneath a given winding due to tile gap requirements, and this also affects OL. Therefore, the C2a design variable is set so that OL is initially 20 % of the X-axis winding pitch and adjusted by ±5 % to identify k_{null}.

C3 has minimal impact on $k_{2a,2b}$. However, decreasing C3 results in higher self-inductance by increasing the Winding Pitch Y. It also lowers $\Delta k_{1,2(eff)}$ by reducing the maximum coupling, but lowers $k_{1,2(eff)}$ under misalignment. Solutions with a larger C3 were favored as, higher $k_{1,2(eff)}$ requires less volt-ampere effort, more evenly distributes magnetic flux density throughout the ferrite core ($B_{ferrite}$), and requires less copper volume (average turn length is decreased).

The number of turns required in both the L_{2a} and L_{2b} windings (N_s) was estimated using the single-turn inductance of each candidate solution as predicted by FEA. Care was taken to estimate that the inter-winding spacing was sufficient based on the C3 and C4a/b winding widths. Setting the number of turns (N_s) to 7 produced candidate solutions within range of the ideal self-inductance of 28.8 µH, while leaving freedom to adjust winding widths and sufficient spacing between successive turns.

Leakage flux adjacent to the EV ($B_{leakage}$) (See Fig. 1), and magnetic flux within the ferrite core ($B_{ferrite}$) were estimated under rated volt-amperes in the GA and VA magnetics under

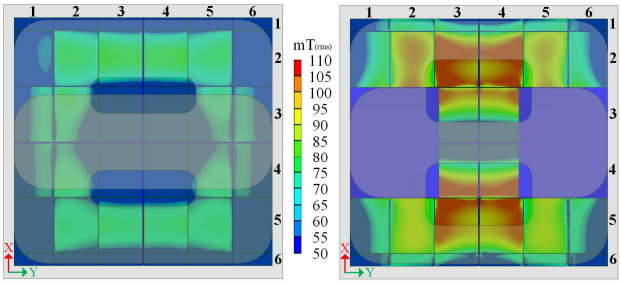

Fig. 6. FEA $|B|$ contour plot at rated volt-amperes for full ferrite design (a), and reduced ferrite design (b).

maximum misalignment/airgap conditions. Design solutions with a wide C3 winding width produced low $B_{leakage}$ due to the Y-axis winding pitch being further from the leakage flux detection plane. A wide C3 winding width also spreads $B_{ferrite}$ more evenly so these solutions were generally favored.

B. Alternative Ferrite Core Structures

TDK N95 ferrite was selected as the magnetic core material due to its high permeability, reasonably low-loss at 85 kHz, and ability to operate with $|B|$ = 200 mT (rms) without saturation occurring [33]. These characteristics assist with creating a compact and efficient magnetics design with minimal leakage flux. Modern powder cores or nanocrystalline materials may also be viable, however for the purposes of this work and to keep the design comparable with literature listed in Tables I and XII (see Section VII), ferrite was preferred.

The ferrite core is made from N95 125x100x10 mm tiles, and based on previous works [32], the tiles were oriented vertically, and small inter-tile gaps were used to reduce magnetic flux hotspots. A conservative maximum ($B_{ferrite,max}$ as per Table I), of $|B|$ = 90 mT was chosen as the prototype BPP VA was designed without active cooling.

Two ferrite core structures were proposed for the BPP design as per Fig. 6. The first is a full ferrite design (FFD) (Fig. 6(a)). The second is a reduced ferrite design (RFD), which has tiles (3,1) and (3,2) symmetrically removed as per Fig. 6(b). Apart from a reduced ferrite core volume, the RFD is able to reduce the inherent increase in pad thickness due to the overlap of L_{2a} and L_{2b} coils required to achieve $k_{2a,2b} < 0.01$. In the cavities left by ferrites (3,1) and (3,2), the coils are able to be placed almost co-planar with the ferrite layer and therefore, the increased pad thickness due to the overlap in this region is reduced.

Both the FFD and RFD were simulated under maximum misalignment and WPT5 rated volt-ampere conditions (I_{2m} = 130 A rms). The internal ferrite $|B|$ contour plots are shown in Fig. 6. While the RFD has a reduced pad profile, the reduced ferrite volume increases $|B|$ and the amount of uneven flux distribution within the core.

The reduced ferrite BPP design could be viable for a similar WPT5 IPT system with a lower airgap and higher coupling (therefore less volt-ampere effort), or a system that is able to actively cool the magnetics. For the requirements in this work the full ferrite core BPP design is the best fit solution.

C. L_{2a} and L_{2b} Winding Overlap Techniques

As discussed in [9], [12], [18], and shown by Fig. 4(a)

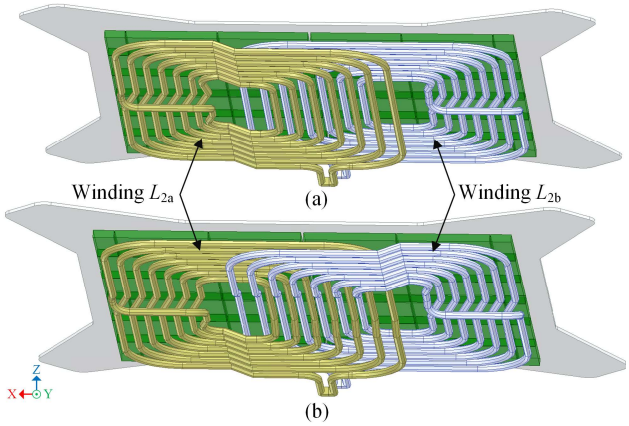

Fig. 7. Detailed FEA models of BPP VA L_{2a} and L_{2b} overlap methods. Folded (a), woven (b).

TABLE V
WPT3/5 BPP VA COIL OVERLAP METHOD COMPARISON

	$k_{1,2(\text{eff})\text{min}}$	$\Delta k_{1,2(\text{eff})}$	$k_{2a,2b}$	$L_{2a} - L_{2b}$
Folded	0.123	0.105	< 0.01	1.1 µH
Woven	0.122	0.103	< 0.01	0.1 µH

through (b), and Fig. 7(a), the simplest method of overlapping L_{2a} and L_{2b} to achieve $k_{2a,2b} < 0.01$ is to have one coil lay flat against the ferrite core (L_{2b} as per figures), and the other coil (L_{2a}) folded over the front.

An alternative method is shown in Fig. 7(b) where L_{2a} and L_{2b} are each folded once below the other on either side of the pad. Both coils are then woven together to lay flat against the ferrite core along the center Y-axis of the pad.

Table V compares the magnetic behavior of the two coil winding methods predicted by a detailed FEA simulation. The results show little difference in coupling behavior. However, there is a 1.1 µH self-inductance difference between the folded and overlap method.

For a commercial system, the folded overlap technique may be preferred due to its simplicity in mass manufacturing. The difference in self-inductance could be mitigated by intentionally mistuning both windings for the midpoint between L_{2a} and L_{2b} or having two sets of tuning network values.

For the prototype WPT3/5 BPP magnetics presented in this work, the woven method was chosen to keep the L_{2a} and L_{2b} tuning networks identical and allow a similar winding current and volt-ampere effort during WPT5 operation.

D. Coupling Performance of Candidate BPP Solutions

Attempting to manipulate a viable WPT5 solution to closely resemble WTP3 specifications in SAE J2954 results in poor performance under both charging conditions. The best approach was to keep $k_{1,2(\text{eff})\text{min}}$ and $\Delta k_{1,2(\text{eff})}$ low during the WPT5 stage of the BPP design process (Fig. 5). As the WPT5 GA and WPT3 UGA are both CP topologies, these desirable coupling characteristics carry through to WPT3 operation.

Table VI shows the k_{min} and k_{max} positions and respective coupling for the proposed BPP VA when operating over the WPT5 GA. The $k_{1,2(\text{eff})\text{min}}$ and $\Delta k_{1,2(\text{eff})}$ performance meets the WPT5 specifications as per Table II. The system was tested experimentally at both the k_{min} and k_{max} positions and results are

TABLE VI
COUPLING FACTORS FOR WPT3/5 BPP VA OVER WPT5 GA AND WPT3 UGA

WPT5 GA

Position	(dx,dy,dz) (mm)	$k_{1,2a}$	$k_{1,2b}$	$k_{1,2(\text{eff})}$	$\Delta k_{1,2(\text{eff})}$
k_{max}	(0,0,160)	0.163	0.162	0.230	0.106
k_{min}	(-75,-100,210)	0.111	0.055	0.124	

WPT3 UGA

Position	(dx,dy,dz) (mm)	$k_{1,2a}$	$k_{1,2b}$	$k_{1,2(\text{eff})}$
1	(0,0,160)	0.262	0.257	0.367
2	(-75,0,160)	0.331	0.113	0.350
3	(-75,-100,210)	0.191	0.069	0.203

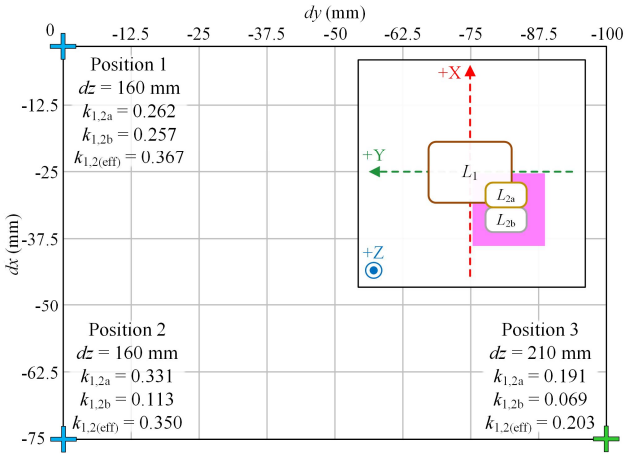

Fig. 8. Alignment map for WPT3/5 BPP VA over WPT3 UGA. Subfigure shows a zoomed out overhead view of the magnetics (not to scale), and highlights in the pink the quadrant/region depicted by the grid map.

presented in Section VII.

When the BPP VA is placed above the circular WPT3 UGA with SCE assisted operation, the k_{min} and k_{max} positions no longer correspond to the aligned and fully misaligned positions. This is due to the poles of the BPP VA being offset to achieve k_{null}. Therefore, k_{min} and k_{max} will change depending on which BPP coil is chosen to transfer power over a given range of VA alignments. Table VI demonstrates three VA alignment positions which are of interest, and these are shown in Fig. 8.

Position 1 aligns the BPP VA over the UGA. This represents a challenging operating point where both L_{2a} and L_{2b} are highly coupled to the UGA. If SCE were unavailable, both BPP coils would receive power (i.e. the coupling of the system would be $k_{1,2(\text{eff})}$), which results in impractical system operation similar to the single-coil WPT5 CP attempting to charge from the WPT3 UGA (as shown previously in Table III). This position is investigated later in Section VII where the application of SCE and the proposed control method demonstrates a significant improvement in operating characteristics.

Position 2 represents another challenging operating point where there is significant asymmetry in the coupling of L_{2a} and L_{2b} with the UGA caused by the dx misalignment as per Fig. 8. Assuming SCE is available, selecting L_{2a} would require a higher power regulation effort (due to the higher coupling), while selecting L_{2b} would require a lower power regulation effort (due to the lower coupling). Both options are explored in Section VII to compare how the loss is distributed throughout

the magnetics and power electronics for each scenario.

Position 3 represents the operating point where the BPP VA is fully misaligned from the UGA as shown by the green cross in Fig. 8. Similar to Position 2, both L_{2a} and L_{2b} exhibit asymmetrical coupling to the UGA. However, the difference in coupling is less significant and is lower in magnitude. Position 2 better demonstrates a challenging operating point with asymmetrical coupling and was preferred for experiments.

IV. Power Regulation Method One: Conduction Angle (α) Control

For most WPT3 charging systems, power regulation can be performed by conduction angle control (referred to as α-control) of the GA active bridge. However, for the showcased WPT3/5 interoperable system, GA side α-control is insufficient to perform power regulation on its own (as demonstrated in Section VI). Zero-Voltage Switching (ZVS) is also discussed in the following sub-sections.

A. Conduction Angle (α-Control) Power Regulation

A diagram of the GA active bridge is shown in Fig. 9(a). The CAS120M12BM2 MOSFET modules (S_1 through S_4) are shown with gate drive circuitry and parasitic capacitances masked. Fig. 9(b) shows a diagram of the bridge voltage and current waveforms (V_{b1} and I_{b1}) and marks the turn on currents for S_1 and S_3 ($I_{S1(on)}$ and $I_{S3(on)}$).

The phase shift between S_1 and S_3 is referred to as the conduction angle (α_1). Controlling α_1 regulates power by controlling the rms magnitude of the first harmonic component of V_{b1} which has been proven in previous literature [34]. In an LCC system, this controls the magnitude of I_1 and hence the volt-amperes in the GA magnetics [23], [35].

Ideally, α_1 can be controlled from 180° down to almost 0° to regulate power flow. However, there are practical limitations which restrict the minimum α_1. The main restriction is ZVS in the active bridge.

B. Zero-Voltage Switching (ZVS)

Maintaining ZVS conditions for an active bridge over the majority of its operating range is challenging for an IPT system, but provides many benefits. Switching losses are reduced under ZVS conditions (increasing efficiency), so less heat needs to be dissipated, enabling cheaper switch modules and lowering heat sinking requirements.

Hard-switching (non-ZVS) results in increased EMI, which can interfere with signal processing and control circuitry (additional shielding expense), and reduces the operational life of the switch modules.

ZVS is most easily achieved when α_1 is close to 180°. As α_1 decreases, the third harmonic content in I_{b1} decreases and the switch begins to transition under a higher fundamental harmonic current [26], [28], [34], [36]. As such, it is difficult to simply use α-control to regulate the power flow as a practical inverter will begin to hard-switch. This causes excess loss and EMI which is undesirable.

Despite this, hard-switching must be tolerated if volt-ampere regulation is needed. It is critical to ensure that the allowable hard-switching currents are considered by choosing the most cost-effective switches, ensuring good thermal design, and considering proper EMI shielding.

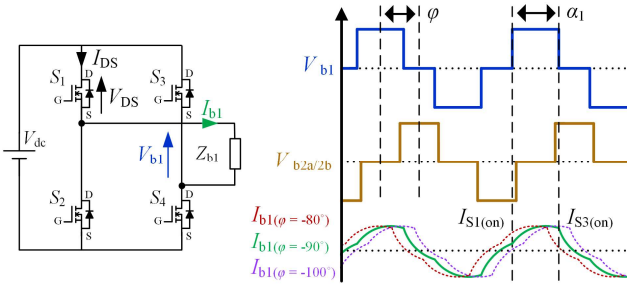

(a) (b)

Fig. 9. (a) GA bridge showing output voltage, current, and output impedance. (b) Timing diagram example of VA bridge lagging GA bridge by 90° (φ = -90°), GA and VA bridge conduction angles at 120° and 100° respectively (α_1 = 120°, α_2 = 100°) as per equation (16). Bottom plot shows phase shift of GA bridge current I_{b1} as φ is varied.

V. Power Regulation Method Two : Active Bridge Phase Shift (φ) Control

An alternative or supplemental method to conduction angle control (α-control) is to control the phase shift between the switching actions of the VA and GA active bridges (φ-control).

Unlike α-control, which regulates the volt-ampere effort of the GA and/or VA magnetics to regulate power, φ-control maintains near constant volt-amperes in the system.

Under φ-control, the power factor of the IPT system, and hence real power transfer, is managed by manipulating the phase angle of the impedance observed by the GA and VA active bridges. This comes at the expense of cycling a high level of reactive power, which results in loss disproportionate to the amount of real power transferred [24], [37].

The following sub-sections discuss the mechanisms of φ-control and demonstrate its ability to assist in maintaining ZVS by controlling the reflected impedance of the candidate WPT3/5 interoperable system.

A. Active Bridge Phase Shift (φ-control) Power Regulation

φ-control manipulates the phase shift between the ac voltage waveforms of the GA and VA active bridges, i.e. V_{b2a} and V_{b2b} with respect to V_{b1} as per Fig. 2 & Fig. 9(b). These phase shift control variables are defined as $\varphi_{Vb1,Vb2a}$ and $\varphi_{Vb1,Vb2b}$.

φ-control subsequently controls the phase shift of currents I_{2a} and I_{2b} with respect to I_1, defined as $\theta_{I1,I2a}$ and $\theta_{I1,I2b}$ respectively. As per (4) in Section II, this allows bi-directional power transfer and power regulation [26].

In this work, when power is delivered by using both VA active bridges, they are made to operate at the same φ-control angle (φ). Therefore, the phase of I_{2a} and I_{2b} with respect to I_1 will be almost equal and defined as θ. As the LCC-LCC system is not perfectly tuned (because of parasitic reactance/resistance, component tolerances etc.), θ will usually be a few degrees lower in magnitude compared to φ.

B. First Harmonic Analysis of Dual Active Bridge Loading

A first harmonic simplification of the LCC tuned system is used to demonstrate the characteristics of the impedance

reflected onto the GA active bridge and show how controlling θ (via φ-control), can improve ZVS performance.

A simplified electrical diagram of the GA system is shown previously in Fig. 9(a), which depicts the output impedance of the active bridge as Z_{b1} described by (15). The reflected impedance of the VA system (Z_{2r}) is represented by (16), and the 85 kHz resonant impedance of the GA side LCC network (X_{L1eff}) is shown by (17). This first harmonic simplification of LCC-LCC active bridge loading is provided in greater detail in previous works [39].

$$Z_{b1} = \frac{X_{L1eff}^2}{Z_{2r}} e^{-j(\theta+90°)} \quad (15)$$

$$Z_{2r} = \frac{V_{oc2,1}}{I_1} = \frac{\omega M_{2,1} I_2}{I_1} e^{j(\theta+90°)} \quad (16)$$

$$|X_{L1eff}| = |X_{LCL1}| = |j\omega L_{LCL1}| \quad (17)$$

As discussed in the previous sub-section, θ in (15) is directly controlled by φ, and therefore φ-control can be used to control the reactive loading of Z_{b1}. From (15), (θ + 90°) will be greater than 0° if -90° < φ < 0°. Therefore, capacitive loading will appear on the GA active bridge. However if φ < -90°, inductive loading will occur.

This control concept was first explored in [24] for a series tuned system with dual active bridges, and was shown to increase efficiency depending on coupling factor conditions. This was later demonstrated in [25] using a matched (with an identical GA and VA), LCC tuned system where the efficiency of the system could be improved when power regulation was required.

C. Advantages of φ-control and φ-Overdrive

As discussed in the previous sub-sections, in an LCC-LCC tuned system, manipulating φ not only regulates power flow and direction, but shifts the phase of I_{b1} to either lag (with inductive loading) or lead (with capacitive loading) V_{b1}. This effect is shown in the I_{b1} current plots of Fig. 9(b).

As φ is moved to -80° to regulate power flow, I_{b1} will begin to lead V_{b1} as the resulting Z_{b1} in (15) becomes increasingly capacitive, increasing $I_{S1(on)}$ (red plot in Fig. 9(b)). This results in an increase in the hard-switching losses in the GA active bridge. Moving φ to -80° limits the minimum α_1 that can be used for conduction angle power regulation if ZVS operation is required.

Another approach, referred to in this work as φ-overdrive, is to instead move φ past -90° with φ becoming increasingly negative. An example is shown in Fig. 9(b) (the purple plot), where φ = -100°. This has the same power regulation effect as φ = -80°, except I_{b1} will now lag V_{b1}, and $I_{S1(on)}$ will decrease to almost zero. This is demonstrated in the following sections to be beneficial when moderate power regulation is required, such as power class interoperability, as it allows a greater range of α-control while maintaining ZVS.

VI. Proposed α + φ-Overdrive Control Method and Experiment Setup

As discussed in previous sections, dual-side control provides flexibility in power regulation. For this work, three control variables are used: α-control in both the GA and VA (α_1, α_2) and φ-control (φ).

As discussed in Section II-E, SCE is used in cases where the WPT3 UGA is present. $k_{1,2m}$ is estimated based on $I_{sc(eff)m}$ readings and low bandwidth communication with the GA control system. Consequently either L_{2a} or L_{2b} is selected to transfer power while the other remains shorted.

The following sub-sections discuss how these three power regulation control variables and SCE can produce a practical WPT3/5 interoperable system. The control algorithm used to derive the control input combinations is provided and the experimental setup for the interoperable system verification is presented (Fig. 10 and Fig. 11 respectively).

A. Limitations of GA Side α-Control

Table VII and Fig. 12 demonstrate why power regulation using only GA side α-control cannot provide the power regulation flexibility necessary for a WPT3/5 interoperable system. Table VII column one states the GA rating (WPT3 for the 10 kW UGA, WPT5 for the 50 kW CP), while columns two and three show the VA alignment position and coupling values for each simulation.

The WPT3 simulation (Table VII Row 1 and Fig. 12 (a)), aligns the BPP VA and UGA (as per Position 1 in Fig. 8), and demonstrates WPT3 power transfer with only GA side α-control power regulation with SCE disabled (and therefore coupling is equal to $k_{1,2(eff)}$). The simulated results and

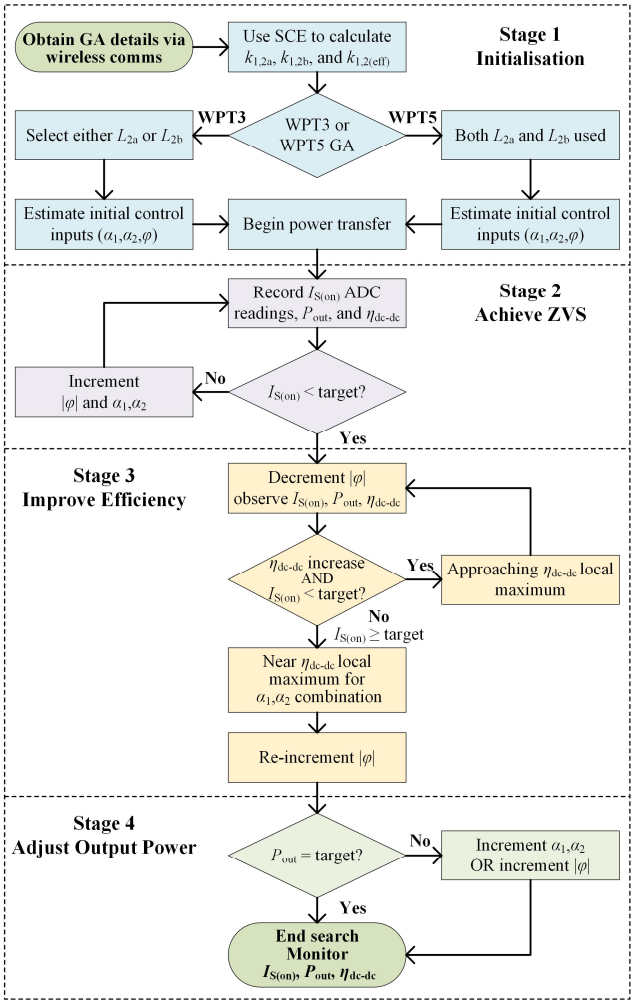

Fig. 10. Controller flowchart used to identify control input combinations.

TABLE VII
PROPOSED BPP VA CHARGING FROM WTP3 UGA AND WPT5 (GA SIDE α-CONTROL ONLY) PLECS SIMULATION CHARACTERISTICS*

GA Rating	(dx,dy,dz) (mm)	$k_{1,2(\text{eff})}$	P_{out} (kW)	$(\alpha_1, \alpha_2, \varphi)$ (°)	V_{dc} (V)	I_1 (A)	I_{2a} (A)	I_{2b} (A)	I_{b1} (A)	I_{b2a} (A)	I_{b2b} (A)	GA $I_{S(on)max}$ (A)	Q_{2max}
WPT3	(0,0,160)	0.367	10.5	(18,180,-90)	380	58.4	128.5	128.5	234.7	40.7	40.6	320.8	1.1
WPT5	(0,0,160)	0.230	50.1	(92,180,-90)	600	105.7	133.4	134.0	139.2	40.4	40.8	115.9	8.8

*V_{batt} = 800 V

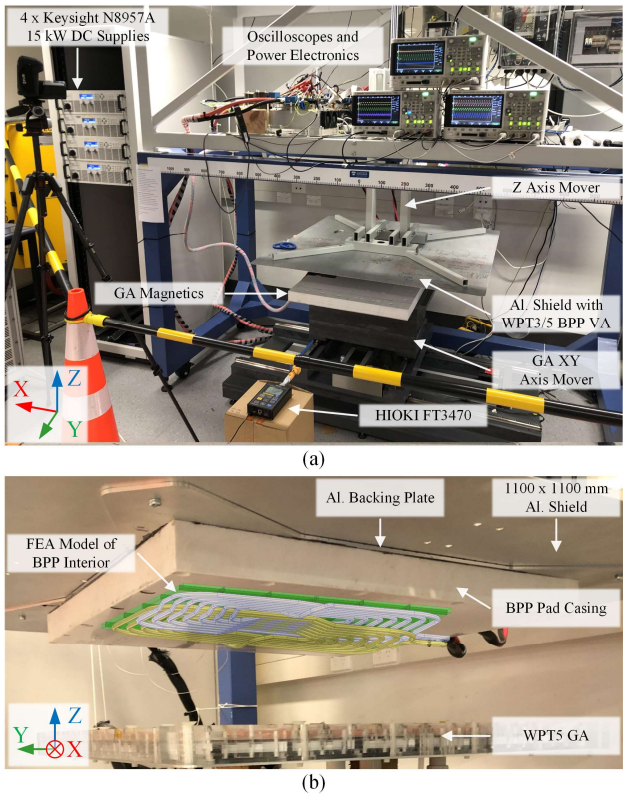

Fig. 11. (a) Experiment setup with WPT3 UGA transferring rated power to WPT3/5 BPP VA. (b) WPT3/5 BPP VA over WPT5 GA.

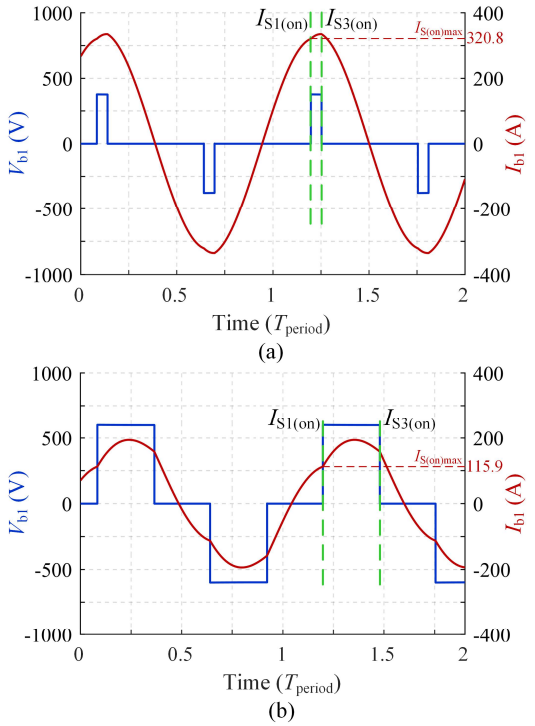

Fig. 12. Simulated ac bridge voltage (blue) and current (red) waveforms as per Table VII. Green dashes mark S_1 and S_3 switching transitions where $I_{S(on)}$ is recorded. (a) Sim 1 WPT3 GA active bridge (b) Sim 2 WPT5 GA active bridge.

waveforms in Table VII show an unrealistic level of α-control (α_1), is required which results in an excessive bridge current (I_{b1}) and level of hard-switching ($I_{S(on)max}$), outside reasonable operating conditions of a WPT3 rated active bridge. The high magnitude bridge current and high level of hard-switching is depicted in the simulated waveforms of Fig. 12(a).

The high coupling also produces a loaded Q_2 factor that is almost equal to 1, which presents similar issues to the example given in Section II-F where a single-coil WPT5 VA attempts to charge from the WPT3 UGA. The unregulated volt-amperes of the BPP VA also decreases system efficiency and this is explored further in Section VII.

The WPT5 simulation (Table VII Row 2 and Fig. 12 (b)), aligns the WPT3/5 BPP VA over the WPT5 GA using GA side α-control under high coupling conditions. The simulation results and waveforms show it operates with high I_{b1} and excessive $I_{S(on)max}$. This results in high inverter losses, both conduction and switching, and introduces significant EMI into the system.

Section VII demonstrates how the addition of SCE (for WPT3 operation), combined with α+φ-control, achieves practical operating conditions for these otherwise inoperable VA alignment and power transfer conditions.

B. *Proposed α+φ-control Experimental Combinations*

Combinations of (α_1, α_2, φ) control inputs can be used to reduce hard-switching in both the GA & VA active bridges, reduce conduction losses in both the magnetics and electronics, and overall increase system efficiency when regulating power.

V_{dc} on the GA can also be adjusted within its operating range to regulate power. However, this work examines the extreme operating conditions of the proposed system, where V_{dc} will be at its minimum value when power regulation is required.

PLECS simulations were used to test (α_1, α_2, φ) input combinations for WPT3 and WPT5 operation. Table VIII lists the combinations that were chosen to showcase the proposed WPT3/5 BPP VA.

The scope of this work does not include a feedback control system that derives optimal control input combinations. The objective here was to demonstrate the effectiveness of the control strategy and the combination of multi-coil SCE and α+φ-control with φ-overdrive to facilitate power class interoperability. The feedback control uses a perturb and observe method and the algorithm is described by the flowchart shown previously in Fig. 10.

The control algorithm relies on feedback regarding output

power (P_{out}), dc-dc efficiency ($n_{dc\text{-}dc}$), and the switching currents ($I_{S(on)}$), in the active bridges. The prototype active bridges use a Current Transformer (CT) on the ac output (see dotted lines in Fig. 2), as an over current safety feature. This signal is also fed into the ADC of the bridge controller which records $I_{S(on)}$ in time with the output pulse width modulation signals that drive the respective switches.

As the system is LCC tuned, this CT can be used to detect changes in bridge current magnitude caused by changes in coupling during charging. This may occur as an EFV is loaded or unloaded and the ride height (dz) changes. The control algorithm can compensate by readjusting the control input combinations to achieve the required power throughput.

For the purposes of this work synchronization of the DAB system was achieved using a wired connection which is also used in relevant IPT literature [25], [30], [38]. Existing literature demonstrates wireless synchronization methods which would be suitable for this application [26], [31], [37].

Stage 1 and Stage 2 of Fig. 10 initializes the system under a set of default control inputs (α_1, α_2, φ) which are decided based on the controllability of the GA, then (α_1, α_2, φ) are incremented until ZVS is achieved in the GA, or, in both the GA and VA.

Stage 3 fine tunes the (α_1, α_2, φ) combination to operate the system near a $n_{dc\text{-}dc}$ local maximum while maintaining ZVS, and Stage 4 checks the system is operating at the desired power level.

TABLE VIII
CONTROL INPUT COMBINATIONS CHOSEN FOR EXPERIMENTAL VERIFICATION OF PROPOSED WPT3/5 BPP VA

		WPT3			
Experiment	$k_{1,2a/b}$	V_{dc} (V)	α_1	α_2	φ
EX1	0.113 ($k_{1,2b}$)	380	120°	92°	-90°
EX2	0.331 ($k_{1,2a}$)	380	120°	28°	-90°
EX3	0.262 ($k_{1,2a}$)	380	120°	36°	-90°
EX1P	0.113 ($k_{1,2b}$)	380	120°	115°	-120°
EX2P	0.331 ($k_{1,2a}$)	380	120°	40°	-135°
EX3P	0.262 ($k_{1,2a}$)	380	120°	58°	-140°
		WPT5			
Experiment	$k_{1,2(eff)}$	V_{dc} (V)	α_1	α_2	φ
EX4	0.124	800	180°	180°	-90°
EX5	0.230	600	120°	110°	-90°
EX5P	0.230	600	130°	130°	-120°

This flowchart was used to derive the (α_1, α_2, φ) control input combinations for the experiments in Tables VIII and IX which demonstrate the α+φ-control method when φ is driven past -90°.

C. WPT3/5 BPP VA Experiment Setup

The experimental setup is shown in Fig. 11, which makes use of an automated IPT pad alignment system. Four Keysight N8957A 15 kW DC supplies are connected in parallel and source up to 60 kW of power. A Regatron G5.54.1000.162-RSS-22078 is used to model the 800 V EV battery (V_{batt}) and can sink up to 54 kW of power.

The maximum leakage flux was measured by a HIOKI FT3470 leakage flux probe (see bottom of Fig. 11(a)), for WPT3 and WPT5 worst case leakage flux conditions. Component values for the tuning networks and prototype magnetics are displayed in Table X with respect to Fig. 2.

VII. EXPERIMENT RESULTS AND DISCUSSION

The WPT3/5 interoperable BPP VA system presented in this work was prototyped and tested in a laboratory setting. The experiments demonstrate the proposed interoperable BPP VA can receive rated power from a WPT3 UGA and WPT5 GA under aligned and misaligned conditions while meeting design specifications.

All measured results are summarized in Table IX and are discussed in the following sub-sections. For the WPT3 experiments, EX1 through EX3 demonstrate dual-sided α-control, while those with a "P" suffix (EX1P through EX3P), demonstrate the same experiments but using the α+φ-control method. For the WPT5 experiments, only EX5 and EX5P require power regulation.

To examine the effectiveness of the α+φ-control method, Table XI provides an approximate breakdown of the losses in the system for WPT3 experiments EX1P, EX2, and EX2P. Fig. 13 provides oscilloscope captures showing the turn on current ($I_{S(on)}$) for each leg of the main active bridges for these three experiments.

Table XII also provides a loss breakdown of the WPT5 maximum coupling experiments EX5 and EX5P to demonstrate the improvements provided by the α+φ-control at high-power.

TABLE IX
EXPERIMENTAL RESULTS FOR VERIFICATION OF PROPOSED WPT3/5 BPP VA (SEE TABLE VIII FOR CONTROL INPUTS)

							WPT3					
Experiment	P_{out} (kW)	$\eta_{dc\text{-}dc}$ (%)	*SCE*	I_1 (A)	I_{2a} (A)	I_{2b} (A)	I_{b1} (A)	I_{b2a} (A)	I_{b2b} (A)	GA $I_{S(on)max}$ (A)	VA $I_{S(on)max}$ (A)	$B_{leak(max)}$ (μT)
EX1	9.70	88.0	L_{2b}	59.7	-	95.6	39.4	63.1	25.7	35.0	18.8	4.1
EX2	10.15	89.0	L_{2a}	59.2	33.8	-	40.5	63.7	19.9	37.5	67.5	4.4
EX3	10.79	89.5	L_{2a}	60.4	43.6	-	43.0	52.5	50.0	41.3	41.2	2.8
EX1P	9.54	88.5	L_{2b}	53.5	-	111.3	37.3	57.5	17.7	8.8	8.0	4.3
EX2P	9.96	92.4	L_{2a}	48.7	46.3	-	45.0	51.9	17.0	-58.8	20.0	2.7
EX3P	10.42	93.1	L_{2a}	47.7	64.7	-	48.4	40.3	40.4	-68.3	-88.4	2.4
							WPT5					
Experiment	P_{out} (kW)	$\eta_{dc\text{-}dc}$ (%)	*SCE*	I_1 (A)	I_{2a} (A)	I_{2b} (A)	I_{b1} (A)	I_{b2a} (A)	I_{b2b} (A)	GA $I_{S(on)max}$ (A)	VA $I_{S(on)max}$ (A)	$B_{leak(max)}$ (μT)
EX4	49.15	94.0	$L_{2a/b}$	198.9	131.6	132.4	75.2	48.3	29.8	-73.8	-38.8	12.3
EX5	50.47	93.2	$L_{2a/b}$	129.1	111.2	111.4	113.9	44.5	45.7	50.0	31.5	6.1
EX5P	50.44	93.9	$L_{2a/b}$	123.7	121.7	121.7	127.4	40.2	39.9	-162.0	-44.2	5.1

TABLE X
MEASURED COMPONENT VALUES/PARAMETERS (SEE FIG. 2) FOR WPT3 AND WPT5 EXPERIMENTS

WPT3 UGA		WPT5 GA		BPP VA	
L_1	40.5 µH	L_1	18.0 µH	$L_{2a/b}$	25.2 µH
$L_{1(lead)}$	1.3 µH	$L_{1(lead)}$	2.0 µH	$L_{2a/b(lead)}$	0.7 µH
C_{1s}	122 nF	C_{1s}	263 nF	C_{2s}	228 nF
C_{1p}	356 nF	C_{1p}	520 nF	C_{2p}	342 nF
L_{LCL1}	12.3 µH	L_{LCL1}	7.5 µH	L_{LCL2}	10.7 µH

A. Loss Estimation Methods

Tables XI and XII estimated losses are based on a combination of device and material datasheets, and LCR measurements. The Equivalent Series Resistance (ESR) measured from the LCC capacitor tuning boards (made up of TDK C0G ceramic capacitors), has been demonstrated to be reasonably constant with temperature and provide accurate loss estimations [40]. For the LCC tuning inductors and IPT magnetics, the ESR information provided by the LCR meter captured the coil winding losses which was supplemented by FEA predicted magnetic core losses under power transfer conditions.

The conduction and switching losses within the CAS120 switch modules while operating at a switching frequency of 85 kHz were estimated using lookup tables derived from the device datasheet. The case temperature of the modules was measured to estimate the junction temperature to provide a more accurate estimation.

The most significant error in these loss estimations is attributed to the estimated magnetics losses being roughly 20 % lower than what would be measured using a power analyzer [41]. For the purposes of this work the trends in these estimated losses agreed with the overall predicted shift in system efficiency observed by the experiment results.

B. BPP VA to WPT5 (50 kW) GA Experiment Results

EX4 demonstrates the BPP VA transferring 50 kW of power under worst under maximum misalignment and ground clearance ((*dx*,*dy*,*dz*) = (-75,-100,210) mm). Under these low coupling conditions power regulation is not required, however, both the GA & VA active bridges are synchronized with φ = -90°. The measured efficiency is 94.0 %, which is comparable to the 94.9 % efficiency of the synchronized WPT5 CP-CP system [37].

TABLE XI
ESTIMATED LOSS (W) BREAKDOWN FOR WPT3 EXPERIMENTS

GA Losses	EX1P	EX2	EX2P
Switching	84.8	125.2	68.6
Total Bridge	129.2	177.7	133.5
Magnetics	120.3	147.2	99.6
Tuning Network	22.6	23.8	20.4
Total	272.2	348.6	253.5
VA-A Losses			
Switching	-	442.0	309.4
Total Bridge	168.6	573.5	396.5
Magnetics	-	34.3	64.3
Tuning Network	54.1	51.7	35.4
Total	222.6	659.5	496.2
VA-B Losses			
Switching	85.0	-	-
Total Bridge	95.2	46.2	38.7
Magnetics	371.7	-	-
Tuning Network	35.6	8.5	5.8
Total	502.5	54.7	44.5
Estimated Loss	997.3	1062.8	794.1
Measured Loss	1240.0	1250.0	820.0
Measured Efficiency	88.5 %	89.0 %	92.4 %

Under maximum coupling ((*dx*,*dy*,*dz*) = (0,0,160) mm), hard-switching occurs in experiment EX5 if only α-control power regulation is used ($I_{S(on)max}$ as per Table IX). EX5P adds α+φ-control which ensures ZVS on both the GA and VA and improves system efficiency by 0.7 %. This can be observed by considering the loss breakdown of the two experiments provided in Table XII, which shows a significant reduction in switching losses in the VA active bridges.

The maximum leakage flux adjacent to the experiment ($B_{leak(max)}$), measured as per Fig. 1 was approximately 12.1 µT and aligns well with the FEA predicted 12.3 µT as per Table IX (see Appendix for supplemental media demonstration). WPT5 EX5P shows a decrease in $B_{leak(max)}$ when compared with WPT5 EX5, which shows α+φ-control also reduces leakage flux in addition to increasing system efficiency.

These results show the proposed system can operate at the WPT5 power class, while Table XIII compares this performance against existing high-power IPT systems in the literature. Comparing the WPT5 operation of the proposed interoperable system with the referenced 50 kW single-coil system (which guided the design boundaries in Section II of this article), shows the proposed BPP VA operates with comparable efficiency and functionality.

The key benefits of the proposed system are in its wireless power class interoperability functionality. Its low-power operation is discussed in the following sub-section.

C. BPP VA to WPT3 (10 kW) UGA Experiment Results

EX1/1P both demonstrate the BPP VA under misalignment at (*dx*,*dy*,*dz*) = (-75,0,160) mm (Fig. 8, Position 2), while transferring full power via L_{2b}. This demonstrates a scenario where low coupling ($k_{1,2b}$ = 0.113) is selected via SCE and less power regulation effort from the VA electronics is required.

Under the same misalignment, SCE may alternatively transfer power through the highly coupled L_{2a} ($k_{1,2a}$ = 0.331) which is shown by EX2/2P. This requires more power

TABLE XII
ESTIMATED LOSS (W) BREAKDOWN FOR WPT5 EXPERIMENTS

GA Losses	EX5	EX5P
Switching	344.3	242.3
Total Bridge	749.0	731.7
Magnetics	389.9	383.5
Tuning Network	313.8	328.1
Total	1452.7	1443.4
VA Losses (Combined)		
Switching	549.1	195.5
Total Bridge	678.7	305.5
Magnetics	706.3	848.9
Tuning Network	288.9	282.4
Total	1673.9	1436.8
Estimated Loss	3126.5	2880.2
Measured Loss	3670.0	3294.0
Measured Efficiency	93.2 %	93.9 %

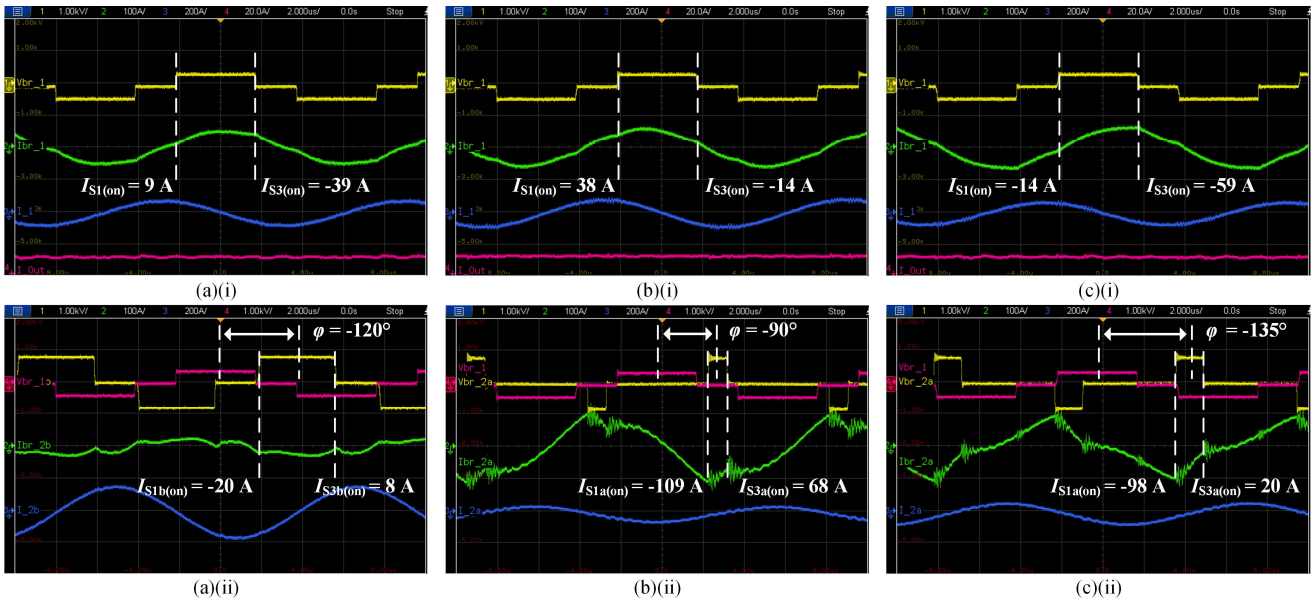

Fig. 13. Oscilloscope switching waveform captures for: WPT3-EXP1P GA active bridge (a)(i) and VA active bridge (a)(ii). WPT3-EXP2 GA active bridge (b)(i) and VA active bridge (b)(ii). WPT3-EXP2P GA active bridge (c)(i) and VA active bridge (c)(ii).

regulation from the VA active bridge but reduces the volt-amperes in the magnetics.

Comparing the EX1/1P and EX2/2P results in Table IX show α+φ control is able to increase efficiency by 0.5 % under low coupling, while selecting high coupling produces a larger efficiency increase of 3.4 %. The reduced effectiveness of α+φ-control in EX1P is due to the high $I_{sc(eff)}$ circulated through the shorted active bridge A (I_{b2a}), which is largely unaffected by the control effort on the active coil L_{2b}. The high coil current (I_{2b}), and therefore high volt-amperes in the VA magnetics, cause the magnetic loss to dominate the breakdown of EX1P as shown in Table XI. This is a practical example of the challenges faced when attempting to operate over such a power class range (WPT3 to WPT5).

The results suggest selecting the higher coupled L_{2a} (EX2P), produces a more efficient system at the expense of a higher control effort by reducing the hard-switching in the GA and VA active bridges. Fig. 13 (b)(i) and (c)(i) shows the addition of φ-control under high coupling reduces the switching losses by manipulating the output impedance of the GA active bridge. This reduces $I_{S(on)}$ without any change to conduction angle α_1.

Comparing Fig. 13 (b)(ii) & (c)(ii) also shows a reduced $I_{S(on)}$ in the VA active bridge, where the added power regulation of the φ-control allows less α-control, which further lowers the switching losses.

Comparing the EX1P and EX2P results also demonstrates the predictability of the required control inputs to achieve rated power transfer. Operating with a lower coupling (EX1P), requires less α-control (i.e. a higher conduction angle), and requires less φ-control to lower the switching currents in the active bridges. The opposite behavior is observed in EX2P which requires a higher control effort to account for the increased coupling. This predictability of the system is used to select the initial control input combination in Stage 1 of the control flowchart shown previously in Fig. 11.

Experiments EX3/3P investigates the BPP VA when it is centered over the UGA ((*dx,dy,dz*) = (0,0,160) mm), as shown previously in Fig. 8 as Position 1. As discussed in Section II-F and Section VI-A, this alignment position is virtually inoperable using only VA or GA side power regulation due to the high coupling and the volt-ampere mismatch of the UGA and VA.

EX3 demonstrates that with SCE and dual-sided α-control the system can now operate at the aligned position, however, the hard-switching in the active bridges ($I_{S(on)max}$) is still excessive and the efficiency ($\eta_{dc\text{-}dc}$) is below 90 %.

EX3P applies α+φ-control, and enables ZVS in both the GA and VA active bridges to improve the system efficiency by 3.6 %. This demonstrates the effectiveness of the proposed combination of SCE with α+φ-control to facilitate WPT3 operation of a WPT5 rated multi-coil VA.

Table XIII compares the WPT3 power transfer performance with existing low-power IPT systems in the literature, and demonstrates comparable system efficiency under similar operating conditions.

Leakage flux under WPT3 operation for EX1 was measured at 3.9 µT which agrees with the FEA predicted 4.1 µT (see Appendix for supplemental media demonstration). In general the results show that α+φ-control will decrease leakage flux, with exception of WPT3 EX1 and WPT3 EX1P, which is due to the SCE choice.

VIII. Conclusions

This article presents an SAE WPT3/5 (10/50 kW) power class interoperable multi-coil BPP VA with a dual-side control strategy for IPT charging of EVs. Challenges associated with operation over a wide range of power classes are discussed and recommendations are made how they can be addressed through multi-coil magnetics design, selective coil energization, and power control strategies.

Experiments demonstrated the proposed interoperable BPP VA charging at rated power from an SAE J2954 WPT3 UGA

TABLE XIII
COMPARISON OF PROPOSED WPT3/5 SYSTEM WITH EXISTING LOW-POWER AND HIGH-POWER IPT SYSTEMS

Institution	Power Level (kW)	Tuning Topology	Magnetic Topology	Efficiency $\eta_{dc\text{-}dc}$ (%)	Alignment dx,dy (mm)	Airgap (dz) mm	Year
Low-Power Systems							
NPU, [42]	7	LCC	DDP	93	(0,0)	200	2014
ORNL [43]	12	Series-Parallel	CP	95	(0,0)	162	2016
WiTricity [44]	3-11	Various	CP	91-93	(0,0)	100-250	2016
ORNL [45]	11	N/A	BPP	92	(0,0)	150	2016
SAE [1]	3-11	Various	CP,DDP	> 80-85	(±75, ±100)	100-250	2020
Proposed System	10	LCC	BPP	92-93	(±75, ±100)	160-210	2023
High-Power Systems							
ETH [8]	50	Series	CP,DDP	95 96	(±100,0) (0,0)	160	2016
UoW, UoC [46]	50	LCC-Parallel	DDP	89	(0,0)	200	2019
ORNL [13]	50 10	Series	3-Phase	95 87	(0,0) (±100, ±100)	170	2020
ORNL [47]	50	LCC	3-Phase	94	(0,0)	150	2021
ZJU [14]	50	Series	3-Phase	95	(0,0)	160	2021
UoA [32],[37]	50	LCC	CP	95 94	(±75, ±100) (0,0)	210 160	2022
Proposed System	50	LCC	CP,BPP	94 94	(±75, ±100) (0,0)	210 160	2023

and WPT5 CP developed in previous works. Low coupling and high coupling power transfer conditions were used to demonstrate the functionality of the proposed α+φ-control method with selective coil energization.

Results demonstrate an efficiency increase of 3.6% and 0.7 % at WPT3 and WPT5 rated power transfer levels respectively.

APPENDIX

Supplemental media provides a video demonstration which can be found at https://youtu.be/6k2rvpkO-Zk, which demonstrates the WPT3 EX1 and WPT5 EX1 system operation and measured leakage flux.

REFERENCES

[1] *Power Transfer for Light-Duty Plug-in/Electric Vehicles and Alignment Methodology*, SAE J2954, 2020

[2] S. Y. R. Hui, W. Zhong and C. K. Lee, "A Critical Review of Recent Progress in Mid-Range Wireless Power Transfer," in *IEEE Transactions on Power Electronics*, vol. 29, no. 9, pp. 4500-4511, Sept. 2014

[3] J. M. Miller and A. Daga, "Elements of Wireless Power Transfer Essential to High Power Charging of Heavy Duty Vehicles," in *IEEE Transactions on Transportation Electrification*, vol. 1, no. 1, pp. 26-39, June 2015

[4] H. Feng, R. Tavakoli, O. C. Onar and Z. Pantic, "Advances in High-Power Wireless Charging Systems: Overview and Design Considerations," in *IEEE Transactions on Transportation Electrification*, vol. 6, no. 3, pp. 886-919, Sept. 2020

[5] N. Mohamed et al., "A Comprehensive Analysis of Wireless Charging Systems for Electric Vehicles," in IEEE Access, vol. 10, pp. 43865-43881, 2022, doi: 10.1109/ACCESS.2022.3168727.

[6] G. A. Covic and J. T. Boys, "Modern Trends in Inductive Power Transfer for Transportation Applications," in *IEEE Journal of Emerging and Selected Topics in Power Electronics*, vol. 1, no. 1, pp. 28-41, March 2013

[7] M. Budhia, J. T. Boys, G. A. Covic and C. -Y. Huang, "Development of a Single-Sided Flux Magnetic Coupler for Electric Vehicle IPT Charging Systems," in *IEEE Transactions on Industrial Electronics*, vol. 60, no. 1, pp. 318-328, Jan. 2013, doi: 10.1109/TIE.2011.2179274.

[8] R. Bosshard, U. Iruretagoyena and J. W. Kolar, "Comprehensive Evaluation of Rectangular and Double-D Coil Geometry for 50 kW/85 kHz IPT System," in *IEEE Journal of Emerging and Selected Topics in Power Electronics*, vol. 4, no. 4, pp. 1406-1415, Dec. 2016

[9] A. Zaheer, H. Hao, G. A. Covic and D. Kacprzak, "Investigation of Multiple Decoupled Coil Primary Pad Topologies in Lumped IPT Systems for Interoperable Electric Vehicle Charging," in *IEEE Transactions on Power Electronics*, vol. 30, no. 4, pp. 1937-1955, April 2015, doi: 10.1109/TPEL.2014.2329693.

[10] S. Y. Jeong, S. Y. Choi, M. R. Sonapreetha and C. T. Rim, "DQ-quadrature power supply coil sets with large tolerances for wireless stationary EV chargers," 2015 IEEE PELS Workshop on Emerging Technologies: Wireless Power (2015 WoW), Daejeon, Korea (South), 2015, pp. 1-6, doi: 10.1109/WoW.2015.7132800.

[11] H. Matsumoto, Y. Neba, H. Iura, D. Tsutsumi, K. Ishizaka and R. Itoh, "Trifoliate Three-Phase Contactless Power Transformer in Case of Winding-Alignment," in *IEEE Transactions on Industrial Electronics*, vol. 61, no. 1, pp. 53-62, Jan. 2014, doi: 10.1109/TIE.2013.2242421.

[12] S. Kim, G. A. Covic and J. T. Boys, "Comparison of Tripolar and Circular Pads for IPT Charging Systems," in *IEEE Transactions on Power Electronics*, vol. 33, no. 7, pp. 6093-6103, July 2018, doi: 10.1109/TPEL.2017.2740944.

[13] J. Pries, V. P. N. Galigekere, O. C. Onar and G. Su, "A 50-kW Three-Phase Wireless Power Transfer System Using Bipolar Windings and Series Resonant Networks for Rotating Magnetic Fields," in *IEEE Transactions on Power Electronics*, vol. 35, no. 5, pp. 4500-4517, May 2020

[14] A. U. Ibrahim, W. Zhong and M. D. Xu, "A 50-kW Three-Channel Wireless Power Transfer System With Low Stray Magnetic Field," in *IEEE Transactions on Power Electronics*, vol. 36, no. 9, pp. 9941-9954, Sept. 2021

[15] W. Zhang, J. C. White, A. M. Abraham and C. C. Mi, "Loosely Coupled Transformer Structure and Interoperability Study for EV Wireless Charging Systems," in *IEEE Transactions on Power Electronics*, vol. 30, no. 11, pp. 6356-6367, Nov. 2015, doi: 10.1109/TPEL.2015.2433678.

[16] G. Yang et al., "Interoperability Improvement for Wireless Electric Vehicle Charging System Using Adaptive Phase-Control Transmitter," in *IEEE Access*, vol. 7, pp. 41365-41379, 2019, doi: 10.1109/ACCESS.2019.2907741.

[17] T. Kurpat and L. Eckstein, "A Three-Phase Inductive Power Transfer Coil with SAE J2954 WPT3 Magnetic Interoperability," *2019 IEEE PELS*

Workshop on Emerging Technologies: Wireless Power Transfer (WoW), London, UK, 2019, pp. 150-155, doi: 10.1109/WoW45936.2019.9030687.

[18] D. Kraus and H. -G. Herzog, "Magnetic Design of a Q-Coil for a 10 kW DDQ System for Inductive Power Transfer," *2019 IEEE PELS Workshop on Emerging Technologies: Wireless Power Transfer (WoW)*, London, UK, 2019, pp. 140-143, doi: 10.1109/WoW45936.2019.9030643.

[19] A. C. Bagchi, A. Kamineni, R. A. Zane and R. Carlson, "Review and Comparative Analysis of Topologies and Control Methods in Dynamic Wireless Charging of Electric Vehicles," in *IEEE Journal of Emerging and Selected Topics in Power Electronics*, vol. 9, no. 4, pp. 4947-4962, Aug. 2021, doi: 10.1109/JESTPE.2021.3058968.

[20] G. -J. Su, M. Mohammad and V. P. Galigekere, "Interoperability between Three-Phase and Single-Phase WPT Systems," *2023 IEEE Wireless Power Technology Conference and Expo (WPTCE)*, San Diego, CA, USA, 2023, pp. 1-6, doi: 10.1109/WPTCE56855.2023.10215837.

[21] I. -M. Torres-Alfonso et al., "An Interoperable 50 kW Inductive Power Transfer Design for Opportunity Wireless Vehicle Charging," *PCIM Europe 2023; International Exhibition and Conference for Power Electronics, Intelligent Motion, Renewable Energy and Energy Management*, Nuremberg, Germany, 2023, pp. 1-10, doi: 10.30420/566091102.

[22] H. H. Wu, G. A. Covic, J. T. Boys and D. J. Robertson, "A Series-Tuned Inductive-Power-Transfer Pickup With a Controllable AC-Voltage Output," in IEEE Transactions on Power Electronics, vol. 26, no. 1, pp. 98-109, Jan. 2011, doi: 10.1109/TPEL.2010.2052069.

[23] H. H. Wu, A. Gilchrist, K. D. Sealy and D. Bronson, "A High Efficiency 5 kW Inductive Charger for EVs Using Dual Side Control," in *IEEE Transactions on Industrial Informatics*, vol. 8, no. 3, pp. 585-595, Aug. 2012, doi: 10.1109/TII.2012.2192283.

[24] Lei Zhao, D. J. Thrimawithana, U. K. Madawala and C. A. Baguley, "Performance optimization of LC bi-directional inductive power transfer system," *2015 IEEE 13th Brazilian Power Electronics Conference and 1st Southern Power Electronics Conference (COBEP/SPEC)*, Fortaleza, 2015, pp. 1-6, doi: 10.1109/COBEP.2015.7420297.

[25] X. Zhang et al., "A Control Strategy for Efficiency Optimization and Wide ZVS Operation Range in Bidirectional Inductive Power Transfer System," in *IEEE Transactions on Industrial Electronics*, vol. 66, no. 8, pp. 5958-5969, Aug. 2019, doi: 10.1109/TIE.2018.2871794.

[26] Y. Tang et al., "A New Controller for Bidirectional Wireless Power Transfer Systems," in *IEEE Transactions on Power Electronics*, vol. 33, no. 10, pp. 9076-9087, Oct. 2018, doi: 10.1109/TPEL.2017.2785365.

[27] G. R. Kalra, D. J. Thrimawithana, B. S. Riar, C. -Y. Huang and M. Neuburger, "A Novel Boost Active Bridge-Based Inductive Power Transfer System," in IEEE Transactions on Industrial Electronics, vol. 67, no. 2, pp. 1103-1112, Feb. 2020, doi: 10.1109/TIE.2019.2898615.

[28] H. Hu, T. Cai, S. Duan, X. Zhang, J. Niu and H. Feng, "An Optimal Variable Frequency Phase Shift Control Strategy for ZVS Operation Within Wide Power Range in IPT Systems," in *IEEE Transactions on Power Electronics*, vol. 35, no. 5, pp. 5517-5530, May 2020, doi: 10.1109/TPEL.2019.2947092.

[29] M. Wu et al., "A Dual-Sided Control Strategy Based on Mode Switching for Efficiency Optimization in Wireless Power Transfer System," in *IEEE Transactions on Power Electronics*, vol. 36, no. 8, pp. 8835-8848, Aug. 2021, doi: 10.1109/TPEL.2021.3055963.

[30] M. Mohammad et al., "Bidirectional LCC–LCC-Compensated 20-kW Wireless Power Transfer System for Medium-Duty Vehicle Charging," in IEEE Transactions on Transportation Electrification, vol. 7, no. 3, pp. 1205-1218, Sept. 2021, doi: 10.1109/TTE.2021.3049138.

[31] Y. Zhang, X. Li, S. Chen and Y. Tang, "Soft Switching for Strongly Coupled Wireless Power Transfer System With 90° Dual-Side Phase Shift," in *IEEE Transactions on Industrial Electronics*, vol. 69, no. 1, pp. 282-292, Jan. 2022, doi: 10.1109/TIE.2021.3055158.

[32] P. A. J. Lawton, F. J. Lin and G. A. Covic, "Magnetic Design Considerations for High-Power Wireless Charging Systems," in *IEEE Transactions on Power Electronics*, vol. 37, no. 8, pp. 9972-9982, Aug. 2022, doi: 10.1109/TPEL.2022.3154365.

[33] TDK, "SIFERRIT material N95", N95, Feb. 2023.

[34] N. Mohan, T. M. Undeland, and W. P. Robbins, Power Electronics: Converters, applications, and design. Hoboken, NJ: John Wiley & Sons, 2003.

[35] S. Zhou and C. C.Mi, "Multi-paralleled LCC reactive power compensation networks and their tuning method for electric vehicle dynamic wireless charging," *IEEE Trans. Ind. Electron.*, vol. 63, no. 10, pp. 6546–6556, Oct. 2016, doi: 10.1109/TIE.2015.2512236.

[36] F. Lin, P. A. J. Lawton and G. A. Covic, "Discrete Modelling of Passive Rectifiers in LCL Tuned Inductive Power Transfer Receivers," in IEEE Transactions on Power Electronics, doi: 10.1109/TPEL.2023.3272645.

[37] P. A. J. Lawton, F. J. Lin, G. A. Covic and D. J. Thrimawithana, "A Wireless Synchronization Controller for High-Power Stationary and Semi-Dynamic Wireless Charging of Electric Vehicles," in *IEEE Transactions on Power Electronics*, vol. 38, no. 11, pp. 13341-13352, Nov. 2023, doi: 10.1109/TPEL.2023.3302281.

[38] T. Li et al., "Enhancing V2G Applications: Analysis and Optimization of a CC/CV Bidirectional IPT System with Wide Range ZVS," in IEEE Transactions on Transportation Electrification, doi: 10.1109/TTE.2024.3369079.

[39] P. Lawton, F. J. Lin and G. Covic, "A Dual Sided Power Regulation Control Strategy for a 50 kW Inductive Power Transfer EV Charger," 2024 IEEE Wireless Power Technology Conference and Expo (WPTCE), Kyoto, Japan, 2024, pp. 806-810, doi:10.1109/WPTCE59894.2024.10557441.

[40] A. K. Bailey, J. Wong, S. Kim, W. Wijaya and G. A. Covic, "Thermal Modelling of Resonant Capacitor Boards for Inductive Power Transfer Systems," 2024 IEEE Wireless Power Technology Conference and Expo (WPTCE), Kyoto, Japan, 2024, pp. 173-176, doi: 10.1109/WPTCE59894.2024.10557396.

[41] G. R. Kalra, M. G. S. Pearce, S. Kim, D. J. Thrimawithana and G. A. Covic, "A Power Loss Measurement Technique for Inductive Power Transfer Magnetic Couplers," in *IEEE Journal of Emerging and Selected Topics in Industrial Electronics*, vol. 1, no. 2, pp. 113-122, Oct. 2020.

[42] J. Deng, Fei Lu, S. Li, T. -D. Nguyen and C. Mi, "Development of a high efficiency primary side controlled 7kW wireless power charger," *2014 IEEE International Electric Vehicle Conference (IEVC)*, Florence, Italy, 2014, pp. 1-6, doi: 10.1109/IEVC.2014.7056204.

[43] O. C. Onar, S. L. Campbell, L. E. Seiber, C. P. White and M. Chinthavali, "A high-power wireless charging system development and integration for a Toyota RAV4 electric vehicle," *2016 IEEE Transportation Electrification Conference and Expo (ITEC)*, Dearborn, MI, USA, 2016, pp. 1-8, doi: 10.1109/ITEC.2016.7520247.

[44] "The Next Wireless Revolution: Electric Vehicle Wireless Charging Power and Efficiency," WiTricity, https://witricity.com/hubfs/videos/WiTricity-Power-and-Efficiency.pdf (accessed 2024).

[45] M. Mohammad, O. C. Onar, J. L. Pries, V. P. Galigekere, G. -J. Su and J. Wilkins, "Analysis of Magnetic Field Emissions and Shield Requirements for Interoperating High-Power EV Wireless Charging System," *2021 IEEE Applied Power Electronics Conference and Exposition (APEC)*, Phoenix, AZ, USA, 2021, pp. 1586-1592, doi: 10.1109/APEC42165.2021.9487265.

[46] A. Ridge, K. K. Ahamad, R. McMahon and J. Miles, "Development of a 50 kW Wireless Power Transfer System," *2019 IEEE PELS Workshop on Emerging Technologies: Wireless Power Transfer (WoW)*, London, UK, 2019, pp. 406-409, doi: 10.1109/WoW45936.2019.9030672.

[47] M. Mohammad, O. C. Onar, J. L. Pries, V. P. Galigekere, G. -J. Su and J. Wilkins, "Thermal Analysis of a 50 kW Three-Phase Wireless Charging System," *2021 IEEE Transportation Electrification Conference & Expo (ITEC)*, Chicago, IL, USA, 2021, pp. 1-6, doi: 10.1109/ITEC51675.2021.9490053.

Patrick A. J Lawton (Student Member, IEEE) received the B.E. (First Class Hons.) degree in electrical and electronic engineering in 2019 from The University of Auckland, Auckland, New Zealand, where he is currently working toward the Ph.D. degree.

His research interests include wireless power transfer for high-power charging of electric vehicles (stationary and semi-dynamic), power class interoperability studies, magnetics design for inductive power transfer systems, power electronics, and control systems.

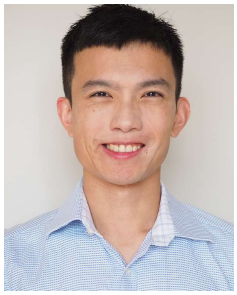

Feiyang (Jackman) Lin (S'14-M'19) received the B.E.(Hons.) and Ph.D. degrees from The University of Auckland, Auckland, New Zealand, in 2012 and 2017, respectively. He is currently a Senior Lecturer with the University of Auckland, working on the design of heavy duty wireless power systems for stationary and dynamic electric vehicle charging applications. During his time as a Research Fellow, he was involved in the design of suitable magnetics to transfer power while meeting safety requirements, as well as the power electronics hardware and software necessary to deliver regulated power safely. He has been involved in developing practical solutions for companies, such as WiTricity and Airbus.

Grant A. Covic (S'88-M'89-SM'04) received his BE (Hons), and PhD degrees in Electrical and Electronic Engineering from The University of Auckland, New Zealand (NZ), where he is now a full Professor within the Department of Electrical, Computer, and Software Engineering Department. He is a co-founder of "HaloIPT" which focused on electric vehicle (EV) wireless charging infrastructure. Before it was on-sold, HaloIPT received the Clean Equity Monaco award for excellence in the field of environmental engineering and two NZ clean innovation awards in the emerging innovator and design and engineering categories. He was awarded the New Zealand Prime Minister's Science Prize, the Vice Chancellors commercialisation medal and the KiwiNet research commercialisation awards for his research, and in 2021 the IEEE Power electronics emerging technology award. He is a Fellow of both Engineering NZ and the Royal Society of NZ, was a Distinguished Lecturer for the IEEE Transportation Electrification Community 2016-2019, and is a co-chair of the steering committee for the IEEE WPTCE conference since 2020. His research and consulting interests include power electronics and resonant inductive power transfer (IPT) from which he has published more than 200 papers in IEEE journals and conferences. He holds more than 50 patent families, from which licenses in specialized application areas of IPT have been granted around the world. Presently he is directing a government funded research program on stationary and dynamic wireless charging of EVs, while also co-leading the interoperability sub-team within the SAE J2954 wireless charging standard.